Multiple rejuvenation episodes of a silicic magma reservoir at the origin of the large diatreme-dome complex and porphyry-type mineralization events at Cerro de Paso (Peru)

Bertrand Rottier[1,2,3,4], Kalin Kouzmanov[3], Maria Ovtcharova[3], Alexey Ulianov[5], Markus Wälle[6†], David Selby[7], and Lluís Fontboté[3]

[1] Département de Géologie et Génie Géologique, Université Laval, Québec, Canada

[2]Centre de recherche sur la géologie et l'ingénierie des ressources minérales (E4m), Québec, Canada

[3]Departement of Earth Sciences, University of Geneva, 1205 Geneva, Switzerland

[4] Bayerisches Geoinstitut, University of Bayreuth, 95440 Bayreuth, Germany

[5]Institute of Earth Sciences, University of Lausanne, 1015 Lausanne, Switzerland

[6]Institute of Geochemistry and Petrology, ETH Zürich, 8092 Zürich, Switzerland

[7]Department of Earth Sciences, University of Durham, Durham DH1 3LE, United Kingdom

[†] present address: Memorial University of Newfoundland, CREAIT, CRC and CFI Services (CCCS), Bruneau Centre for Research and Innovation, St. John's, NL, Canada, A1C 5S7

Corresponding author: bertrand.rottier@ggl.ulaval.ca

Abstract

The Cerro de Pasco district in central Peru hosts one of the world largest porphyry-related epithermal polymetallic deposits. The district is centered onto a large diatreme-dome complex crosscut by numerous dacite to rhyodacite bodies showing domal structures and quartz-monzonite dykes. Three temporally distinct high-temperature porphyry-type mineralization events, preceding the epithermal polymetallic mineralization, have been recognized (PM1, PM2, and PM3). Dating of the latter by molybdenite Re-Os and by zircon U–Pb (LA-ICP-MS and CA-ID-TIMS) geochronology complement the already available dataset of zircon U–Pb ages of the subvolcanic and volcanic rocks from the district. The new geochronology data indicate that the magmatic system was active during more than 400 kyr, spanning from 15.59 ± 0.12 Ma to 15.16 ± 0.04 Ma, punctuated by three porphyry-type mineralization events that are precursors (maximum gap of 0.9 Myr) of the large epithermal polymetallic mineralization at Cerro de Pasco. After detailed petrographic and geochemical (whole rock and minerals) studies, silicate melt inclusions hosted in quartz phenocrysts from the subvolcanic and volcanic rocks emplaced between and after the different porphyry-type mineralization events have been analyzed by LA-ICP-MS. Our results suggest that prior to their emplacement at shallow level, magmas were stored at depth with a high degree of crystallinity (> 50% crystals) at pressures between 0.9 and 3.4 kbar and at temperatures between ~680° and ~725°C. At such conditions, magma is beyond the point of rheological lock-up and is not eruptible. Therefore, the emplacement of the subvolcanic and volcanic rocks has required a series of rejuvenation events of the upper crustal high-crystallinity silicic magma reservoir. Field relationships indicate that emplacement of the subvolcanic and volcanic rocks is preceded by high-temperature (> 600ºC) quartz-pyrite-magnetite ± chalcopyrite and quartz-molybdenite veining forming the three recognized porphyry-type mineralization events. Hydrothermal quartz of these veins host silicate melt inclusions, a rare feature in hydrothermal veins. Their

composition determined by LA-ICP-MS analysis indicates that the mineralizing fluids, potentially sourced from intermediate magma recharges, have circulated in a magma reservoir in which the residual interstitial melt was more evolved than the melt trapped as inclusions in the magmatic quartz. The combined geochemical and geochronological data obtained show that several episodes of rejuvenation of a highly crystallized upper-crustal silicic magma reservoir, probably triggered by intermediate magma recharges, are at the origin of the large diatreme-dome complex and porphyry-type mineralization events at Cerro de Pasco.

Keywords: porphyry; epithermal deposit; zircon; silicate melt inclusions; crystal mush.

Introduction

The vertical extent of porphyry systems, from upper-crustal magma reservoir to near-surface, where epithermal deposits are formed, is between 5 and 15 km (Sillitoe 2010). Reconstruction of the spatial and temporal connection between the different parts of the system (i.e., plutonic intrusions, volcanic bodies, and porphyry and epithermal mineralizations) is complex and requires good knowledge of the magmatic system and geochronological data. During the last decade, several studies have suggested that most intermediate to silicic arc magmas forming large volcanic eruptions or subvolcanic intrusions are sourced from long-lived (several hundred of kyr up to several Myr) upper crustal magma reservoirs (e.g., Bachmann and Bergantz, 2004; Cashman and Blundy, 2013; Cashman et al., 2017; Cooper, 2017; Deering et al., 2016; Schoene et al., 2012; Spark and Cashman, 2017; Szymanowski et al., 2017). Zircon geochronology and thermometry suggest that, during most of their lifetime, these magmas are stored at high-crystallinity degree, under a fundamentally immobile and non-convective state, and at temperatures close to their solidus (e.g., cold storage; Claiborne et al., 2010; Cooper and Kent, 2014; Szymanowski et al., 2017; Wotzlaw et al., 2013). Similar long-lived magmatic systems are associated to porphyry Cu-(Au)-(Mo) deposits, whereas the maximum duration of ore forming events is between few to hundreds of kyr (Buret et al. 2016; Tapster et al. 2016; Large et al., 2018 and 2020). The identification of the processes triggering these short and transient mineralizing events are key to understand the genesis of porphyry Cu-(Au)-(Mo) deposits. Recurrent recharges of less evolved and hotter magmas are required to maintain long-lived (> 100s kyr) upper crustal reservoirs (Cashman et al., 2017; Weber et al., 2020). Indeed, mafic to intermediate magma recharges in magmatic systems associated or not with porphyry Cu-(Au)-(Mo) deposits have been often recognized (e.g., Buret et al., 2016 and 2017; Halter et al., 2004; Hattori and Keith, 2001; Rottier et al., 2019 and 2020; Zhang and Audétat, 2017). The cooling of these newly injected magmas at the contact with the silicic reservoir has the

potential to release magmatic fluids able to trigger volcanic eruptions or to form porphyry Cu-(Au)-(Mo) deposits (Buret et al., 2017; Tapster et al., 2016). Therefore, insight in the timing of porphyry-type mineralization and of shallow magmatic activity is crucial for understanding the magmatic and hydrothermal dynamics at the origin of porphyry systems and of silicic volcanic eruptions.

This work is part of a comprehensive study on the giant porphyry-related epithermal polymetallic deposit of Cerro de Pasco (Baumgartner et al., 2008 and 2009; Rottier et al., 2016a, 2016b, 2018a and 2018b). The present contribution focuses on the temporal and genetic link between volcanic and sub-volcanic rocks, porphyry-type mineralization events, and epithermal polymetallic mineralization at Cerro de Pasco. New CA-ID-TIMS U-Pb zircon geochronology of mineralized magmatic rocks and molybdenite Re-Os geochronology of the different porphyry-type mineralization styles complement previous geochronological work and show the existence of successive short-lived episodes (< 100 kyr) of shallow magmatic activity and porphyry-type mineralization. Alternating magmatic-hydrothermal events is not uncommon in long-lived porphyry systems where mineralized intrusive magmatic dykes crosscut earlier vein generations (e.g., Sillitoe, 2010; Spencer et al., 2015). Comparable alternating volcanic and hydrothermal events is rarely observed (e.g., Buret et al., 2017). The obtained dataset of compositions of silicate melt inclusions hosted in hydrothermal quartz from high-temperature porphyry veins suggest a genetic relationship between the temporally related porphyry-type mineralization and near-surface magmatic activity. The present study shows how several episodes of rejuvenation of a highly crystallized upper-crustal silicic magma reservoir, probably triggered by new injection of intermediate magmas, are at the origin of the large diatreme-dome complex and porphyry-related mineralization events at Cerro de Pasco.

General geology

The Cerro de Pasco district is part of the Miocene metallogenic belt of Peru which includes a large number of polymetallic epithermal, Au-Ag high-sulfidation epithermal, and porphyry Cu-(Mo)-(Au) deposits (Bendezú and Fontboté, 2009; Bissig et al., 2008; Bissig and Tosdal, 2009; Catchpole et al., 2015a; Noble and Mckee, 1999;). The central Peruvian segment of the belt (~10.2-12°S) is part of the flat slab subduction segment of the Andes associated with the subduction of the Nazca ridge that started at 15 Ma (Gutscher et al., 1999, Hampel et al., 2002, Rosembaum et al., 2005). Cenozoic volcanism in the area extends from ~41 Ma to ~5 Ma (Bissig et al., 2008; Bissig and Tosdal, 2009) and is characterized by the emplacement of isolated and small shallow-level intrusions, subaerial domes, and volcanic deposits (Bissig and Tosdal, 2009). Igneous rocks are high-K calc-alkaline and range from basalt to rhyolite, evolved compositions (dacite to rhyolite) being strongly dominant (Bissig and Tosdal, 2009). Central Peruvian ore deposits are genetically associated with this magmatism and show a similar age range from ~39 Ma to ~5 Ma, with a more intense Mid- to Late-Miocene ore formation between 16 Ma and 5 Ma (Noble and McKee, 1999; Bissig and Tosdal, 2009).

District geology and mineralization

The Cerro de Pasco district (Einaudi, 1968; Rogers, 1983; Baumgartner et al., 2008 and 2009; Rottier et al., 2016a, 2016b, 2018a, and 2018b) hosts one of the world largest porphyry-related epithermal polymetallic ("Cordilleran") deposit, with a combined resource of >200 million tons (Mt) at about 7 wt % Zn, 2 wt % Pb, and 3 oz/t Ag in addition to at least 100 Mt at 1.3 wt % Cu and 1 g/t Au (Baumgartner et al., 2008). The geology of the Cerro de Pasco district is dominated by a deformed sedimentary sequence consisting of Devonian slates and phyllites (Excelsior Group), overlain by sandstones and conglomerates of the Middle-Late Triassic Mitu Group (Fig. 1; Rosas et al., 2007; Spikings et al., 2016), covered by up to 1000 m of carbonate rocks belonging to the Late Triassic Chambará Formation, part of the Pucará Group (Angeles,

1999; Baumgartner et al., 2008). Sandstones of the Goyllarizquizga Group (Cretaceous) and limestones and marls of the Pocobamba Formation (Eocene) overlie discordantly the other formations. At Cerro de Pasco, a regional N15° W-striking reverse fault, named Longitudinal Fault juxtaposes the Excelsior Group and the Pucará Group (Fig. 1; Angeles, 1999; Baumgartner et al., 2008).

The diatreme-dome complex of Cerro de Pasco, directly emplaced to the west of the Longitudinal Fault, is 2.5 km in diameter and was formed by a succession of phreatomagmatic and magmatic events (Fig. 1; Baumgartner et al., 2009; Einaudi ,1968; Rogers, 1983; Rottier et al., 2018a). An early phase of explosive activity produced a large diatreme-breccia, mainly composed of stratified and non-stratified breccias known locally as Rumiallana Agglomerate (Rottier et al., 2018a; Fig. 1B). The upper part of the diatreme-breccia consists of a dacitic tuff showing crossbedding and with locally numerous accretionary lapilli (0.2–1 cm in diameter; Rottier et al., 2018a). This tuff outcrops mainly in the southern and subordinately in the northern margins of the diatreme-dome complex (Fig. 1B), Baumgartner et al. (2009) dated one lapilli tuff of this lithology at 15.36 ± 0.03 Ma (zircon U-Pb ID-TIMS). The different facies of the diatreme-breccia are crosscut by volcanic and sub-volcanic intrusions characterized mainly by i) dacite to rhyodacite bodies showing domal structures and emplaced along the western margin of the diatreme breccia, dated at 15.40 ± 0.07 Ma (zircon U-Pb ID-TIMS; Baumgartner et al. 2009); ii) small (each outcrop less than 10x10 m) porphyritic trachyte intrusions in the central part of the diatreme breccia; and iii) E-W trending quartz-monzonite porphyry dykes cutting the diatreme breccia and the dacitic to rhyodacitic magmatic domes (Fig. 1B), two of them were previously dated at 15.35 ± 0.05 Ma and 15.16 ± 0.04 Ma (zircon U-Pb ID-TIMS; Baumgartner et al. 2009). The oldest dated dyke is located in the northern part of the open pit, strikes NE-SW, crosscut the carbonate rocks and is affected by the earliest stages of the epithermal polymetallic mineralization. The youngest dated dyke belongs to the swarm of dykes oriented

E-W which crosscut the porphyritic trachyte intrusions (Figs. 1B and C). Based on the morphology of the diatreme-dome complex and the occurrence of lapilli tuff, the total erosion since the formation of the diatreme-dome complex has been estimated at < 1 km, likely less than 0.5 km (Baumgartner, 2007, Baumgartner et al., 2008; Rottier et al., 2016a and 2018b).

The Cerro de Pasco epithermal polymetallic mineralization is mainly hosted by carbonate rocks along the eastern margin of the diatreme-dome complex (Einaudi, 1977, Baumgartner et al., 2008; Rottier et al., 2018b). It is formed during three successive main mineralization stages (nomenclature and event succession according to Rottier et al., 2016b and 2018b; Fig. 1): A) pipe-like pyrrhotite-dominated bodies grading outwards into Fe-rich sphalerite (up to 80 vol. %) and galena (stage A), B) a large N-S trending funnel-shaped massive pyrite-quartz body with minor hematite (stage B), and C) high-sulfidation mineralization consisting of large well-zoned Zn-Pb-(Bi-Ag-Cu) carbonate replacement ore bodies in the eastern part of the deposit (stage C_1) and a set of E-W–trending Cu-Ag-(Au-Zn-Pb) enargite-pyrite veins hosted by the diatreme breccia (stage C_2).

Description of the dated porphyry-type mineralization occurrences

Three subsequent occurrences of minor porphyry-type mineralization were recognized in the Cerro de Pasco district (Rottier et al.2016a and 2018a), and they have been named PM1, PM2, and PM3 according to the obtained geochronological data. Crosscutting relationships indicate that all porphyry-type mineralization events precede at least stage C_2 of polymetallic epithermal mineralization (for the other polymetallic epithermal stages precise temporal constrains are lacking so far, Rottier et al., 2018a). The first (PM1) and the third (PM3) porphyry-type mineralization events occur as mineralized clasts hosted in the diatreme-breccia and in quartz monzonite dykes, respectively. They represent porphyry-type mineralization formed in the deep part of the system, in contrast to PM2, occurring at a shallower level. The

three porphyry-type mineralization occurrences contain silicate melt inclusions hosted in hydrothermal quartz, which are a major focus of the present study.

Detailed studies on PM1 were performed by Rottier et al. (2018a). It consists of porphyry-type veinlets crosscutting hornfels and porphyritic igneous clasts incorporated in the diatreme-breccia (Fig. 2A, B and C). The quartz-molybdenite-(chalcopyrite)-(pyrite) veinlets are formed at high temperatures (>600°C) and pressures (> 500 bar). Rhyolitic silicate melt inclusions have been found hosted in hydrothermal quartz (Rottier et al., 2018a), like the ones described by Stefanova et al. (2014) at Elatsite porphyry Cu-Au deposit. A molybdenite separate obtained from one large hornfels clasts crosscut by numerous quartz-molybdenite-(chalcopyrite)-(pyrite) veinlets has been dated by the Re-Os geochronology in the frame of the present work.

Porphyry-type mineralization PM2, described by Rottier et al. (2016a), occurs as a network of up to 1 cm-thick quartz-magnetite-chalcopyrite-(pyrite) porphyry veinlets (Fig. 2D) centered on porphyritic trachyte intrusions cropping out in the central part of the diatreme-dome complex (Figs. 1B and C). A quartz-monzonite dyke, previously dated by Baumgartner et al. (2009) at 15.16 ± 0.04 Ma, crosscuts the quartz-magnetite-chalcopyrite-pyrite porphyry veinlets and the trachyte intrusions (see Fig. 2A and 2D in Rottier et al. 2016a). The porphyry veinlets have been formed at low pressure (< 270 bar) in three steps: i) an early high-temperature event (>> 600°C), characterized by inclusions formed by a silicate melt and a hypersaline liquid; ii) a second high-temperature event (>600°C), represented by hypersaline fluid inclusions (~70 wt.% NaCl eq.); and iii) a low-temperature event (<350°C), marked by entrapment of liquid-rich fluid inclusions and sulfide precipitation (Rottier et al., 2016a). One sample of the mineralized porphyritic trachyte has been dated by U-Pb zircon geochronology in the present work.

Porphyry-type mineralization PM3, described by Rottier (2016), occurs as up to 20 cm wide mineralized clasts of porphyritic igneous rocks and hornfels in a quartz-monzonite dyke in the central part of the diatreme dome complex (Figs. 1B and 2D). This dyke belongs to the swarm of E-W striking dykes which crosscut the mineralized trachyte intrusions (PM2) and which was dated by Baumgartner et al. (2009) at 15.16 ± 0.04 Ma (Fig. 1B). Both porphyritic igneous and hornfels clasts are crosscut by a network of quartz-magnetite-chalcopyrite-pyrite veinlets (Fig. 2E). The porphyritic igneous clasts are affected by pervasive silicification and the veinlets display a potassic alteration halo with K-feldspar and shreddy biotite (Fig. 2E). The hornfels clasts are formed by quartz, K-feldspar, minor albite, secondary hydrothermal biotite, and disseminated pyrite and chalcopyrite. As discussed by Rottier (2016), microthermometric analyses of two fluid inclusion assemblages (Supplementary Table A.1) and the high Ti content of the hydrothermal quartz (51-121 ppm, mean = 79 ppm, n=33, LA-ICP-MS data, Supplementary Table A.2) suggest that these veins formed at high temperature (> 600°C) by fluid undergoing phase separation into a low-density vapor and high-salinity brine (> 57 wt% NaCl equiv.). The hydrothermal quartz contains glassy silicate melt inclusions (SMIs) like the ones found in PM1. One porphyritic igneous clast has been dated by U-Pb zircon geochronology in the present work.

Analytical methods

Whole rock

Subvolcanic and volcanic rock samples were collected from surface outcrops (list of samples and their location is available in Supplementary Table A.3). Particular attention was paid on selecting the least altered rock samples. Ten samples were selected for whole rock analysis and were crushed and powdered with an agate mill. Fused glass beads (fluxed with $Li_2B_4O_7$) and pressed powder pellets were analyzed for major, minor, and trace elements by X-

ray fluorescence (XRF) at the University of Lausanne. Additionally, trace elements were analyzed by LA-ICP-MS at the ETH Zurich on fragments of fused glass beads, previously used for XRF analyses.

Petrography, mineral chemistry and silicate melt inclusions

For five representative samples of the subvolcanic and volcanic rocks, automated mineral analysis and textural imaging using a FEI QEMSCAN® Quanta 650F facility at the University of Geneva was performed (detailed analytical method in supplementary file A.1). For the different studied rocks, solid inclusions trapped in minerals were identified by Raman spectroscopy using a confocal LABRAM equipped with a 532.12 -nm Nd-YAG Laser coupled with an Olympus BX51 microscope at the University of Geneva.

Feldspar phenocrysts from selected rocks were analyzed for their major and minor elements. Sodium, Mg, Al, Si, K, Ca, Ti, Mn, Fe, Sr were quantified by electron microprobe analyses (EMPA) using a Jeol JXA 8200 Superprobe WD/ED combined microanalyzer at the University of Lausanne. Quartz grains from representative samples were picked from the size fraction < 2mm and mounted in epoxy. Silicate melt inclusions hosted in quartz phenocrysts were analyzed by LA-ICP-MS at ETH Zurich (detailed analytical method is presented in supplementary file A.1). Suitable SMIs are glassy, between 15 and 40 µm in size and not cropping out at surface after sample preparation. SMIs hosted in hydrothermal quartz from PM3 quartz-magnetite-chalcopyrite veins were analyzed by LA-ICP-MS at the Bayerisches Geoinstitut. Analyzed inclusions were glassy, between 15 and 25 µm in size. Only SMIs that were not spatially associated with fluid inclusions were analyzed in order to avoid possible contamination. All SMIs were quantified following the method of Halter et al. (2002). Internal standardization of melt inclusions was based on SiO_2 vs. MgO or the SiO_2 vs. FeO trends displayed by the whole-rock data. In addition, LA-ICP-MS signals obtained from the analyses of silicate melt inclusions hosted in hydrothermal quartz from PM1 porphyry veins initially

published by Rottier et al. (2018a) have been quantified again following the method described above, as they have been initially quantified by using a fixed the Al_2O_3 content at 16 wt.%. The new quantification method allows a significantly better determination of the major element concentrations (additional information in supplementary file A.1).

Re-Os and U-Pb geochronology

A hornfels clast crosscut by numerous PM1 quartz-molybdenite-(chalcopyrite)-(pyrite) veins (CP-16-BR-X4) sampled in the southeastern part of the diatreme breccia was selected for molybdenite Re-Os geochronology (Fig. 1B). Analysis was conducted at the University of Durham (U.K.) in the TOTAL laboratory for source rock geochronology and geochemistry, following previously published protocols (Selby and Creaser, 2001a, b). Additional details are reported in supplementary file A.1.

A sample of a porphyritic trachyte intrusion affected by the second occurrence porphyry-type mineralization (PM2; CP-14-BR-305) and a clast of porphyritic igneous rock crosscut by veins forming the third occurrence porphyry-type mineralization (PM3; CP-14-BR-X1; Fig. 2E) were selected for U-Pb zircon geochronology. The mineralized (PM3) clast of porphyritic igneous rock was carefully isolated from its host quartz-monzonite dyke to avoid contamination. Zircon grains were separated, handpicked, and mounted in epoxy and polished to expose their internal structure. Prior U-Pb zircon geochronology, an SEM-CL imaging of the zircon crystals was performed. In situ zircon geochronology by LA-ICP-MS was carried out using a Thermo ELEMENT XR sector-field ICPMS interfaced to an UP-193FX ArF excimer laser ablation system at the University of Lausanne following protocols outlined in Ulianov et al. (2012). Zircon displaying homogenous CL textures, no xenocrystic core, and young LA-ICP-MS date were selected for ID-TIMS to resolve the relative emplacement ages of the two rocks; the detailed analytical method is reported in supplementary file A.1. Trace elements composition of selected zircon grains were analyzed by LA-ICP-MS at ETH Zurich.

Results

SEM-CL images and trace element composition of the zircon

SEM-CL images of magmatic zircons from the mineralized porphyritic trachyte intrusion (PM2; n=85 grains) and from the studied mineralized porphyritic igneous clast (PM3; n=78 grains) show euhedral to subhedral crystals with fine well-developed oscillatory and sector zoning (Supplementary Figure A.1). No xenocrystic cores were observed in zircon grains from the mineralized (PM2) trachyte and only two were observed in zircon grains from the mineralized (PM3) clast. Core and rim of a subset of zircon grains from the porphyritic trachyte (n=17) and the mineralized porphyritic igneous clast (n=15) were analyzed by LA-ICP-MS for trace elements (Supplementary Table A.4; Fig. 3). The zircon cores have similar evolution trends marked by a decrease of HREEs, Ce, Th/U ratio in parallel to an increase of the Yb/Dy ratio. According to the mineral abundances of the trachyte porphyry, as determined by QEMSCAN®, the REE budget (except for Eu) of the melt, and thus of the zircon, is controlled at more than 80% by titanite and apatite (Fig. 3B). Determination of the initial mineral abundances of the dated porphyritic igneous clast is not possible due to its strong alteration. Two distinct core-to-rim evolution trends are observed: a “normal evolution” where rims show higher Yb/Dy ratio, lower Ce concentration and strong depletion in HREE compared to the cores which is consistent with the progressive crystallization of titanite and apatite. However, some grains show a “reverse trend” where rims present a lower Yb/Dy ratio and a higher Ce concentration, and only a weak depletion in HREE (Fig. 3C). Zircons having a “reverse evolution” present occasionally resorption textures between the core and the rim of the grains (Fig. 3D).

The Ti content was below the detection limit (Max_{LOD} = 5.4 ppm, Min_{LOD} = 3.1 ppm, $Mean_{LOD}$ = 4.2, n=31), except for three analyses that revealed a Ti content between 3.3 and 3.7

297 ppm (Supplementary Table A.4). Ti-in-zircon thermometer was applied using the calibration of
298 Ferry and Watson (2007) and the limit of detection of Ti was used to determine the maximum
299 crystallization temperature. We used αSiO_2 of 1 because of the presence of quartz in the rocks
300 and αTiO_2 of 0.7 as suggested by Watson et al. (2006) and Fu et al. (2008) for titanite-bearing
301 igneous rocks. A variation of the titanium activity of 0.1 changed the obtained temperatures by
302 ~13ºC. Calculated maximum crystallization temperatures are below 725°C (Max ≈ 722°C, Min
303 ≈ 675 °C, Mean ≈ 700°C, n=31).

304 **Timing of magmatic and high-temperature hydrothermal events**

305 Re-Os geochronology was performed on a molybdenite separate from sulfide-poor
306 quartz-molybdenite-(chalcopyrite)-(pyrite) veins crosscutting a hornfels clast and belonging to
307 PM1. The obtained Re-Os date is 15.59 ± 0.12 Ma (Fig. 4C; the complete data set is available
308 in Supplementary Table A.5).

309 LA-ICP-MS zircon U-Pb ages from the mineralized (PM2) trachyte porphyry and the
310 mineralized (PM3) clast are unimodal indicating that both may represent single zircon
311 populations (Fig. 4A, full dataset is reported in Supplementary Table A.6). The trachyte
312 porphyry (PM2) and the mineralized (PM3) clast yield weighted mean $^{206}Pb/^{238}U$ ages of 14.97
313 ± 0.35 Ma (MSWD = 1.3, n=88) and 14.92 ± 0.35 Ma (MSWD = 1.3, n=56), respectively.

314 High-precision CA-ID-TIMS geochronology was performed on 5 and 7 zircons from
315 the mineralized porphyritic trachyte (PM2) and the mineralized porphyritic igneous clast
316 (PM3), respectively (full dataset is reported in Supplementary Table A.7). This new dataset
317 complements previous zircon geochronology performed by Baumgartner et al. (2009) on one
318 sample of lapilli dacitic tuff, one sample of dacitic dome, and two samples of quartz-monzonite
319 dyke (Fig. 4B). The five zircon crystals from the mineralized porphyritic trachyte (PM2) yield
320 a time range from 15.284 ± 0.009 Ma to 15.439 ± 0.026 Ma (Fig. 4B; Supplementary Table

A.7), the four youngest grains being statistically equivalent (Fig. 4B) and yielding a weighted mean $^{206}Pb/^{238}U$ date of 15.286 ± 0.018 Ma (MSWD = 0.27, n=4). From the 7 zircon grains from the mineralized clast, one was dated at 23.972 ± 0.067 Ma; the remaining 6 grains formed two clusters of three statistically equivalent zircons each (Fig. 4B). The weighted mean $^{206}Pb/^{238}U$ age of the youngest cluster is 15.165 ± 0.043 Ma (MSWD = 1.4, n=3). Both obtained ages are within the uncertainty of the ages obtained by LA-ICP-MS. The weighted mean of the youngest zircons is interpreted to be the best approximation of the emplacement age, considering the rapid cooling of small intrusive bodies upon injection into the sub-volcanic environment (Keller et al., 2018; Large et al., 2020).

Mineral composition and textures of magmatic rocks from the Cerro de Pasco district

Despite the effort to sample the freshest possible outcrops, most analyzed rock samples show a weak hydrothermal alteration marked by the occurrence of fine-grained muscovite, epidote, and chlorite in the samples (Figs. 5 and 6). As shown by Figures 5 and 6, the different rocks are porphyritic with a high content of phenocrysts (> 40 vol. %). All the rocks are characterized by a finely crystallized matrix (< 20 μm) composed dominantly by quartz and K-feldspar, that on the QEMSCAN® mineral maps is sometimes classified as a "Si-K-rich matrix" due to the very small grain size (Figs. 5 and 6). The dacitic tuff, the dacitic domes, and the rhyodacitic domes (rock nomenclature adapted from Baumgartner et al., 2009) have a similar mineralogy, dominated by phenocrysts of plagioclase, biotite, and quartz (Fig. 5A-C). The quartz-monzonite dykes have a similar mineralogy with, in addition, large sanidine phenocrysts (up to 8 cm; Fig. 5D). The porphyritic trachyte intrusion, crosscut by the quartz-magnetite-chalcopyrite-pyrite PM2 stockwork and affected by pervasive chlorite-epidote-sericite-calcite alteration (Fig. 6), consists mainly of phenocrysts of plagioclase, biotite, quartz, and a few phenocrysts of K-feldspar and apatite (Fig. 6). In addition, phenocrysts of hornblende, almost

346 totally replaced by chlorite, are present (Fig. 6). In all rocks, diamond-shaped grains made of
347 leucoxene, ilmenite, and rutile occur; they are interpreted to represent altered titanite
348 phenocrysts. As shown by the calcium maps generated from the QEMSCAN® analyses, most
349 plagioclase phenocrysts of the different rocks are weakly zoned and few of them present
350 resorbed Ca-rich cores (Figs. 5 and 6). EPMA profiles and spot analyses performed on
351 plagioclase from the different rocks reveal limited variation in the anorthite content of the
352 plagioclase phenocrysts (between An_{21} and An_{54} with 94% of the values between An_{21} and
353 An_{30}; n=294; Supplementary Table A.8; Supplementary Figure A.2).

354 A special attention was brought to the sulfur-bearing solid inclusions present in the
355 phenocrysts. Anhydrite and calcite solid inclusions were found in apatite grains in the quartz-
356 monzonite dykes, together with inclusions of quartz, zircon, magnetite (Fig. 7). Both calcite
357 and anhydrite are not spatially associated with cracks or secondary melt or fluid inclusions trails
358 and are considered to be magmatic in origin. The apatite grains are small, between 100 and
359 several 100s of microns, and located in the rock matrix, as shown by the QEMSCAN® calcium
360 maps (Figs. 5 and 6), indicating together with the nature of their solid inclusions (quartz and
361 zircon) that they formed during the late crystallization stage of the rocks. Anhydrite solid
362 inclusions occur in ~5% of the investigated apatite grains. The anhydrite inclusions are euhedral
363 to subhedral, up to 300 µm-long, and generally aligned along apatite growth bands (Fig. 7A).
364 Calcite inclusions are less common than anhydrite and usually form smaller crystals (up to 100
365 µm, Fig. 7A). No anhydrite nor calcite have been identified in the matrix of the quartz-
366 monzonite dykes. No magmatic sulfide inclusions were observed in the studied samples.

367 ## Whole rock geochemistry

368 The Cerro de Pasco magmatic rocks display a narrow range of compositions, mainly
369 dacitic, from 60.6 to 69.7 wt% SiO_2, all rocks are part of the high-K calc-alkaline trend
370 (Supplementary Table A.9). No correlation between the U-Pb ages of the rocks and the

concentrations of any chemical element is observed. Composition of the rocks is similar than the Oligocene and Miocene magmatic rocks from central Peru compiled by Bissig and Tosdal (2008). All the rocks fall in the "adakite" field in the Sr/Y *versus* Y diagram (Fig. 8C) and have an elevated Sr/Y ratio, from 54 to 148 which does not correlate with SiO_2. The primitive mantle normalized spidergram (Fig. 8B) shows well defined Nb and Ta (as well as Y and Ti) negative anomalies and enrichment in large ion lithophile elements (LILE), typical of arc magmas. The REE plot shows a strong depletion of HREE compared to LREE (Fig. 8A), leading to high La/Yb_N ratios (25 to 73). Using the latter criteria, magmatic rocks from Cerro de Pasco also fall in the geochemical "adakite" field in the La/Yb *versus* Yb diagram (Fig. 8D). Rocks also display a strong fractionation between MREE and HREE, illustrated by high Gd/Yb_N ratios (4.2 to 6.6), and a lack of Eu anomaly indicating limited plagioclase fractionation.

Silicate melt inclusions (SMIs) hosted in magmatic quartz

Chemical composition

A total of 33 SMIs hosted in quartz phenocrysts were analyzed by LA-ICP-MS: three from a dacitic tuff (BR-201), four from a dacitic dome (BR-235), 13 from a rhyodacitic dome (BR-230), and 13 from a quartz-monzonite dyke (BR-232 and BR-243; Fig. 9A). No SMIs from the trachyte porphyry and mineralized clasts were analyzed because of the occurrence of numerous secondary fluid inclusions crosscutting the SMIs that made them not suitable for LA-ICP-MS analysis.

The studied SMIs in quartz phenocrysts from the different rocks have similar composition (Figs. 10 and 11). They are rhyolitic, with SiO_2 content between 75.1 and 75.8 wt.%, and K_2O and Na_2O concentrations between 4.8 and 7.2 wt.% and between 2.5 and 4.2 wt.%, respectively (Fig. 10 and Supplementary Table A.10). Compared to whole rock compositions, SMIs are more evolved and are depleted in most compatible elements (e.g., Mg, Fe, Ca, Sr) and enriched in incompatible elements (e.g., K, Rb, Cs, W; Figs. 10 and 11). Metal

contents are coherent with the rhyolitic composition of the SMIs, with values between 2.1 and 26.7 ppm for Cu, between 23.8 and 93.8 ppm for Zn, and between 18 and 48.6 ppm for Pb (Fig. 11). Obtained Cu concentrations should be considered with caution as they can be affected by a post-entrapment diffusion (e.g., Audétat et al., 2018; Lerchbaumer and Audétat, 2012; Rottier et al., 2017). The obtained Cu, Zn, and Pb concentrations are similar to previously published metal contents of SMIs hosted in quartz, plagioclase, amphibole and pyroxene from andesitic to rhyolitic arc magmas (Cu: 9-100 ppm, Pb: 12-105 ppm, Zn: 10-150 ppm; Borisova et al., 2008; Mandeville et al., 1996; Mustard et al., 2006; Nadeau et al., 2013; Price et al., 2005; Johnson et al., 2013; Rottier et al., 2019 and 2020). Molybdenum and W contents range from 1.0 to 9.4 ppm and from 1.8 to 7.5 ppm, respectively (Fig. 11).

Trapping temperature of the silicate melt inclusions were calculated using the zircon saturation thermometers of Watson and Harrison (1983). Zirconium saturation of the melt is indicated by the presence of zircon inclusions in all investigated quartz phenocrysts. Moreover, all SMIs are metaluminous to weakly peraluminous which is another condition required for the application of this thermometer. Typical error range of the zircon saturation thermometer is around 20ºC (Watson and Harrison, 1983). Zircon saturation temperatures range from 680° to 686°C for SMIs from the lapilli dacitic tuff, from 683° to 698 °C for SMIs from the dacitic dome, 684° to 704°C for SMIs from the rhyodacite dome, and from 692° to 722 °C for SMIs from the quartz-monzonite dyke (supplementary table A.10). These low temperatures are coherent with the low Ti content of the zircon grains.

Ti-in-quartz thermobarometry

The Ti-in-quartz thermobarometer was used to obtain insight into pressure conditions during quartz phenocryst crystallization. Calculated pressures were obtained using the thermobarometer developed by Huang and Audétat (2012). The Ti contents of quartz adjacent to each SMI was recalculated using a TiO_2 activity fixed at 0.7 and the temperatures obtained

for each SMI from the zircon saturation thermometry were used. For the lapilli dacitic tuff, pressure ranges from 1.9 to 2.6 kbar (n=3), for the dacitic dome from 2.0 to 2.5 kbar (n=4), for the rhyodacite dome the values are between 2.4 and 3.4 kbar (n=13), and for the quartz-monzonite dyke the values are uniformly distributed between 0.9 and 2.4 kbar (n=13). Calculated pressures are highly sensitive to temperature and to the fixed TiO_2 activity. A temperature variation of ± 20°C (the error range of the zircon saturation thermometer) and a variation of the αTiO_2 of 0.1 induces shifts of the calculated pressure of ~0.5 and of ~0.4 kbar, respectively; therefore, the calculated pressures should be considered with caution. However, all pressure estimations suggest that quartz have crystallized in an upper-crustal magma reservoir.

Silicate melt inclusions hosted in the hydrothermal quartz

The studied silicate melt inclusions are randomly distributed in the hydrothermal quartz crystals from the high-temperature porphyry-type veins. There is no spatial organization of the SMIs inside the veins, and no spatial correlation with fluid inclusions or other solid inclusions (Figs. 9B and C). The SMIs are between 15 and 25 μm in size. They are most of the time glassy, but some are partly crystallized, and few totally crystallized.

Major and trace element compositions of the SMIs hosted in hydrothermal quartz from quartz-molybdenite-(chalcopyrite)-(pyrite) veinlets of PM1 recalculated from Rottier et al. (2018a), and those hosted in hydrothermal quartz from quartz-magnetite-chalcopyrite veinlets of PM3 obtained in this work are presented in Figures 10 and 11, and all data are reported in Supplementary Table A.11. No chemical compositions of SMIs hosted in hydrothermal quartz from PM2 veins are reported because their compositions are affected by co-trapped salt melt inclusions (Rottier et al., 2016a). Nonetheless, EPMA and LA-ICP-MS analyses of the less affected SMIs suggest that trapped melt was rhyolitic (~73 wt.% SiO_2) with a Cs content around

50 ppm (Rottier et al., 2016a, i.e., similar to the composition of the SMIs analyzed in hydrothermal quartz from PM1 and PM3).

In terms of major elements, the analyzed SMIs hosted in hydrothermal quartz from PM1 and PM3 are similar to the ones hosted in magmatic quartz (Fig. 10), whereby, the former show slightly higher Al_2O_3 contents. In terms of trace elements, the SMIs hosted in hydrothermal quartz follow the trend drawn by the whole rock and the SMIs hosted in magmatic quartz for most elements (e.g., Rb, Sr, Cs; Fig. 11). The SMIs hosted in hydrothermal quartz have higher Rb and Cs and lower Sr contents than the SMIs hosted in magmatic quartz (Fig. 11). This indicates that SMIs hosted in hydrothermal quartz are more evolved. The metal contents (Zn, Cu, Pb, Mo and W) are higher in SMIs in hydrothermal quartz than in those in magmatic quartz (Fig. 11C-G). The high values of W and Mo could be attributed to a high evolution degree of the melt, whereas the high contents (up to several 100s of ppm) of Cu, Zn, and Pb are more likely due to the trapping of a unrecognized small volume of metal-rich fluid in the SMIs. These small volumes of metal-rich fluids would only slightly affect the major element composition of the SMIs and of the elements preferentially concentrated in the melt (i.e., Sr and Rb) as illustrated by the fact that, for most elements, the composition of the SMIs follow the trend drawn by the whole rock and the SMIs hosted in magmatic quartz.

Discussion

New geochronological constraints on the hydrothermal mineralization at Cerro de Pasco

Figure 12 presents the age of the three distinct porphyry-type mineralization events in the frame of the magmatic and hydrothermal temporal evolution at Cerro de Pasco. The 15.59 ± 0.12 Ma Re-Os molybdenite age of the first porphyry-type mineralization (PM1) is coherent

468 with the 15.36 ± 0.03 Ma U-Pb zircon age of the dacitic tuff interpreted to be synchronous to
469 the formation of diatreme-breccia that hosts the dated clast (Baumgartner et al., 2009). These
470 two ages suggest a time gap from 380 to 80 kyr between the first porphyry event (PM1) and the
471 oldest dated outcropping magmatic rocks (dacitic tuff and rhyodacite bodies, 15.36 ± 0.03 Ma
472 and 15.40 ± 0.07 Ma, zircon U-Pb ID-TIMS, respectively; Baumgartner et al. 2009; Fig 12).
473 The age of the second porphyry-type mineralization (PM2) is bracketed by the mineralized
474 trachyte porphyry dated at 15.286 ± 0.018 Ma and the crosscutting post-PM2 E-W quartz-
475 monzonite dyke dated at 15.16 ± 0.04 Ma (Baumgartner et al., 2009). Therefore, the maximum
476 lifespan of PM2 mineralization is ~180 kyr (Fig. 12). The age of the last recognized porphyry
477 event (PM3), occurring as mineralized clasts hosted in a quartz monzonite dyke, is bracketed
478 by the age of 15.165 ± 0.043 Ma (MSWD = 1.4, n=3) of the mineralized magmatic clast and
479 that of the host E-W striking quartz-monzonite dyke (15.16 ± 0.04 Ma), i.e., a maximum time
480 span of ~90 kyr (Fig. 12). These ages reveal a period of approximately 400 kyr during which at
481 least three porphyry-type mineralization events alternating with volcanic to sub-volcanic
482 activity took place.

483 According to the available geochronology results, the epithermal polymetallic
484 mineralization of stages A, B, and C has been formed over a maximum lifespan of 1 My,
485 between ~15.4 and ~14.4 Ma (Fig. 12). These constrain are based on the fact that the NE-SW
486 quartz-monzonite dyke dated at 15.35 ± 0.05 Ma (Baumgartner et al., 2009) is affected by the
487 polymetallic mineralization stages A and B and that alunite of the last stage (C_2) yields ages
488 between 14.54 ± 0.06 and 14.41 ± 0.07 Ma (Ar/Ar; Baumgartner et al., 2009). Similar time gaps
489 between magmatic and porphyry Cu-Mo mineralization events and epithermal polymetallic
490 mineralization were observed in other districts such as Morococha (~0.5 Myr; Peru; Catchpole
491 et al., 2015b) and Rosario (~0.7 Myr; Chile; Masterman et al., 2004). The observed time-gap
492 suggests that giant porphyry-related epithermal polymetallic can be formed several hundreds of

493 kyr after the last recognized expression of magmatic or porphyry-type mineralization events
494 (Catchpole et al., 2015b). Significance of this time-gap for the formation of porphyry-related
495 epithermal polymetallic mineralization will require further studies.

496 Magma storage and rejuvenation

497 The temperatures obtained by zircon saturation and the Ti-in-zircon thermometers are
498 similar and indicate that the magma had cooled, prior to its emplacement at sub-volcanic to
499 volcanic level (< 1 km), at temperatures between 675ºC and 725 ºC, i.e., at temperatures close
500 to the water-saturated solidus for a dacitic magma (Caricchi and Blundy, 2015). Even if the
501 storage pressures (between 0.9 and 3.4 kbar) obtained with the Ti-in-quartz thermobarometer
502 should be considered with caution in reason of their large potential errors, the data suggest that
503 quartz phenocrysts have crystallized in an upper-crustal magma reservoir. Finally, the spread
504 of 100 to 300 kyr observed within the single zircon grains of each dated (U-Pb) sample suggests
505 that the magmatic system was active during ~300 kyr and probably reflects continuous zircon
506 growth in a stable zircon-saturated magma reservoir (Fig. 4B). Similar time scales have been
507 proposed for other long-lived and continuously crystallizing magma reservoirs related to
508 porphyry Cu-(Mo)-(Au) deposits such as Bajo de la Alumbrera (241 ± 43 kyr; Argentina; Buret
509 et al. 2016), Koloula (172 ± 115 kyr; Solomon Islands; Tapster et al. (2016); Ok Tedi (212 ±
510 43 kyr; Papua New Guinea; Large et al., 2018), and Batu Hijau (336 ± 27 kyr; Indonesia; Large
511 et al., 2020). Thus, the data suggest that quartz crystals from the sub-volcanic and volcanic
512 rocks have crystallized in a cool, long-lived, upper-crustal magma reservoir. In andesitic to
513 dacitic melts, quartz is among the last phases to crystallize. Therefore, the composition of the
514 SMIs hosted in magmatic quartz provides information on the highest crystallinity degree
515 reached by the magmas in the upper-crustal magma reservoir before their subsequent
516 emplacement at shallower level (< 1 km). At Cerro de Pasco, the studied SMIs hosted in
517 magmatic quartz are more evolved than the composition of their host rocks. This is a common

518 feature in arc-related magmatic rocks (Kent et al., 2010; Lee and Bachmann, 2014; Reubi and
519 Blundy, 2009; Rottier et al., 2019 and 2020) and it can be interpreted as the record of the cooling
520 and crystallization of the injected magmas (andesitic to dacitic) into the upper crustal reservoir
521 (Bachmann and Huber, 2016; Caricchi and Blundy, 2015; Fiedrich et al., 2020; Lee and
522 Bachmann., 2014; Rottier et al., 2020).

523 Cesium is the element that behaves most incompatibly during magma evolution
524 (Audétat and Pettke, 2003; Audétat, 2015 and 2019; Bachmann et al., 2005) and therefore the
525 Cs content of the SMIs can be used as an indicator of the degree of crystallization of a magma.
526 In addition, the partition coefficient of Cs between intermediate-density fluids and evolved
527 silicate melt is relatively small, between 1 to 4 according to Audétat (2019) or even lower,
528 between 0.05 and 0.8 according to Fiedrich et al. (2020). Therefore, Cs content of the melt is
529 only slightly affected by fluid exsolution events. For the studied rocks, the Cs content of the
530 SMIs is between 10.9 and 20.8 ppm, whereas the Cs content of the rocks is between 1.8 and 6.1
531 ppm (Fig. 13B-C). To determine the degree of crystallization of the melt required to produce
532 the Cs content of the SMIs, two models of equilibrium crystallization in a closed system fashion
533 were applied (Fig. 13C). The first one assumes Cs as a totally incompatible element (bulk
534 $Kd^{Cs}_{(mineral+fluid)/melt} = 0$). In the second model, the system was assumed to be fluid-saturated and
535 the water solubility of the melt was fixed at 5 wt.% H_2O which is a good approximation for
536 silicic melts stored in a reservoir at ~2 kbar (e.g., Chelle-Michou et al., 2017). The bulk Kd of
537 Cs was calculated using $Kd^{Cs}_{fluid/melt}$ of 2 (Audétat, 2019), and by using the values $Kd^{Cs}_{mineral/melt}$
538 published by Padilla and Gualda (2016) of biotite ($Kd^{Cs}_{biotite/melt} = 0.43$), plagioclase
539 ($Kd^{Cs}_{plagioclase/melt} = 0.017$), and K-feldspar ($Kd^{Cs}_{K\text{-}feldspar/melt} = 0.013$) for rhyolitic compositions.
540 For each rock, the bulk $Kd^{Cs}_{(mineral+fluid)/melt}$ was calculated using the mineral proportions
541 calculated from the QEMSCAN® mineral maps. The calculated bulk $Kd^{Cs}_{(mineral+fluid)/melt}$ varies
542 between 0.120 and 0.132 for the different rocks. In both models, the Cs content of the whole

543 rock samples was taken as a proxy of the initial Cs concentration of the melt (Fig. 13C). The
544 assumption behind this hypothesis is that the whole rock compositions are a proxy for the melt
545 injected into the upper crustal reservoir. This assumption implies that the crystal cargo carried
546 by the magma was purely autocrystic and that whole rock composition has not been affected
547 by crystal fractionation or by less differentiated magma recharges. The similar plagioclase
548 composition in the different rocks (mostly between An_{21} and An_{30}), the main mineral in the
549 rocks, suggest that these plagioclases are in majority phenocrysts and thus the volume of
550 xenocrysts or antecryst in the rocks is limited (Figs. 5 and 6; supplementary Figure A.2). The
551 possibility that the whole rock compositions were affected by crystal fractionation or magma
552 recharges, and consequently, are not representative of the melt injected into the upper crustal
553 reservoir cannot be discarded. Nonetheless, both cases imply that the composition of the melt
554 injected in the magma reservoir would be more primitive (less Cs-rich) than the ones used in
555 the models (i.e., whole-rock compositions), implying that the calculated crystallinity would be
556 underestimated. Therefore, the obtained degree of crystallinity would be overestimated only if
557 rocks with a higher Cs concentration than the whole-rock compositions are assimilated; this is
558 unlikely regarding the generally low Cs content of crustal rocks (<6 ppm; McLennan, 2001).
559 The constructed models show that between 44 and up to 99 % of crystallization are necessary
560 to reproduce the Cs concentrations measured in the SMIs hosted in the magmatic quartz (Fig.
561 13C). The highest crystallinity (> 99 %) obtained by the above models are too high to be
562 geologically realistic and they probably result from an overestimation of the $Kd^{Cs}_{(mineral+fluid)/melt}$.
563 Despite the different approximations introduced, the constructed models suggest that magmas
564 injected in the upper-crustal reservoir have reached crystallinity > 50% before to form the
565 volcanic and subvolcanic rocks. This high crystallinity is coherent with the evolved
566 composition of the SMIs (Figs. 10 and 11) and also with the low temperatures of crystallization
567 (< 725ºC) obtained from the Zr saturation and Ti-in-zircon thermometers, which are closed to

568 the solidus (Caricchi and Blundy, 2015). Highly evolved melts resulting of this intense
569 crystallization in the upper-crustal reservoir can form interconnected or isolated melt pockets
570 or alternatively formed large evolved melt lenses inside the crystal mush (Bachmann and Huber,
571 2016; Parmigiani et al., 2016). However, eruption of such large evolved melt lenses tends to
572 form crystal-poor rhyolitic rocks (Bachman and Huber, 2016; Parmigiani et al., 2016) that are
573 not consistent with the chemistry and the crystallinity of the subvolcanic and volcanic rocks
574 observed at Cerro de Pasco. Rather, it is proposed that the quartz phenocrysts of the different
575 rocks were formed in a crystal-rich (> 50 %) mush with interstitial highly evolved melt. At
576 crystallinity > 50%, magmas are considered to behave as rigid bodies unable to move through
577 the crust and to erupt (Bachmann and Bergantz, 2004 and 2006; Huber et al., 2010). Thus, a
578 mechanism is required to rejuvenate this reservoir to form the successive emplacement of the
579 sub-volcanic and volcanic rocks at Cerro de Pasco.

580 The three temporally distinct porphyry-type mineralization events (PM1, PM2, and
581 PM3) alternate with the emplacement of sub-volcanic and volcanic rocks (Fig. 12). The study
582 of the SMIs hosted in porphyry-type veins of these mineralization events allows a better
583 understanding of the potential mechanism leading to the rejuvenation of the upper crustal highly
584 crystallized magma reservoir. Silicate melt inclusions in hydrothermal quartz have been
585 observed only in few places (Harris et al., 2003; Ivascanu et al., 2003; Pintea, 1995 and 2014;
586 Rottier et al., 2016a and 2018a; Stefanova et al., 2014). They are interpreted mostly as small
587 droplets of residual melt sampled by hydrothermal fluids during their exsolution and/or
588 circulation in not-totally solidified intrusions (Rottier et al., 2016a and 2018a; Stefanova et al.,
589 2014). In the present study, this interpretation is supported by the fact that major and trace
590 element composition of the SMIs hosted in hydrothermal quartz follow the trend drawn by the
591 composition of the whole rock and of the SMIs hosted in magmatic quartz (Figs. 10 and 11). In
592 addition, this observation suggests that the SMIs and the hydrothermal fluid were in

593 equilibrium, meaning either that the SMIs represent the melts from which the hydrothermal
594 fluid was exsolved or that the fluid has been equilibrated with the evolved melt after its
595 exsolution.

596 The most primitive fluid inclusions found in porphyry veins of PM1 are intermediate-
597 density inclusions that are rich in CO_2 (between 9 and 44 mass %) and sulfur (up to several
598 wt.%; Rottier et al., 2018a). Such fluids are unusually CO_2- and sulfur-rich for intermediate
599 density fluids exsolved from evolved rhyolitic melt (Audétat, 2019; Fiedrich et al., 2020).
600 Considering the average melt composition recorded in the magmatic quartz, a temperature of
601 725ºC, and a pressure of 2 kbar, to exsolve CO_2-rich fluids similar to those trapped in the
602 primitive fluid inclusions (up to 44 mas %), the evolved silicate melt would need to be unusually
603 H_2O-poor (4.2 wt.%) and CO_2-rich (330 ppm; Papale et al., 2006). Moreover, as anhydrite
604 inclusions in apatite were identified, sulfur content of the evolved magmas is buffered by the
605 sulfur concentration at anhydrite saturation (SCAS). The values of SCAS and the coefficient of
606 partition of sulfur between fluid and melt ($Kd^{S}_{Fluid/Melt}$) were calculated using the model Zajacz
607 and Tsay (2019). According, to the model of Zajacz and Tsay (2019), at the conditions
608 described above, the sulfur concentration of the melt and $Kd^{S}_{Fluid/Melt}$ will be 43 ppm and 72,
609 respectively. Thus, fluid exsolved from the highly evolved interstitial melt will have a sulfur
610 concentration ~3500 ppm, which is substantially lower than the sulfur concentrations of the
611 fluid inclusions (up to several wt.%; Rottier et al., 2018a). Therefore, the CO_2- and S-rich
612 intermediate-density fluids are probably not sourced from the highly evolved residual melt.
613 They are interpreted to be sourced from less evolved magma recharges, that crystallized below
614 the silicic crystal mush (Rottier et al., 2018a). These magma recharges are probably close to an
615 andesitic composition according to the whole-rock composition of the volcanic and subvolcanic
616 rocks. Indication of magma recharges in the upper-crustal reservoir is also given by the reverse
617 chemical zonation observed in some zircon grains (Fig. 3C-D) suggesting that episodes of

618 reheating and dissolution of the previously formed titanite (± apatite) happened. Moreover,
619 additional evidence of circulation of CO_2-rich fluids inside the crystal mush is brought by the
620 occurrence of magmatic calcite inclusions in the apatite grains of the quartz-monzonite dykes
621 (Fig. 7).

622 The studied SMIs hosted in hydrothermal quartz are more evolved than those hosted in
623 magmatic quartz (Figs. 10, 11, and 13B-C). The occurrence of these SMIs trapped in
624 hydrothermal quartz from veins of each porphyry-mineralization event indicates that the
625 hydrothermal fluids circulated through a highly crystallized crystal mush before the formation
626 of the porphyry veinlets. As the SMIs hosted in hydrothermal and in magmatic quartz and the
627 whole rock yield similar compositional trends, the CO_2- and S-rich fluids seem to have not
628 affected or only slightly the composition of the SMIs hosted in hydrothermal quartz. This can
629 be explained by the fact that the CO_2- and S-rich fluids have been partly re-equilibrated with
630 the highly evolved melt during their circulation inside the crystal mush. The large compositional
631 range (Figs. 10, 11, and 13B-C) of the SMIs from PM1 veins dated at (15.59 ± 0.12 Ma) is
632 thought to represent the varying compositions of the residual interstitial melt present in a
633 strongly crystallized crystal mush where not connected melt pockets having slightly different
634 compositions coexisted. In contrast, SMIs from PM3 veins, formed later, between 15.286 ±
635 0.018 Ma and 15.16 ± 0.04 Ma, show lower Cs contents and more homogeneous compositions
636 (Figs. 11, and 13B-C), suggesting that during this period the residual melt inside the crystal
637 mush was less evolved and more chemically homogeneous than during the formation of PM1.
638 The occurrence of these SMIs in hydrothermal quartz combined with the close temporal
639 relationship between formation of the porphyry-type mineralization and emplacement of sub-
640 volcanic and volcanic rocks, indicates that circulation of hydrothermal fluids in the highly
641 crystallized magma chamber happened before the emplacement of sub-volcanic and volcanic
642 rocks.

643 The observed alternating formation of porphyry-type mineralization and emplacement
644 of volcanic to sub-volcanic bodies at Cerro de Pasco and the occurrence of silicate melt
645 inclusions in hydrothermal veins of the different porphyry-type mineralization events can be
646 explained by the physical behavior of highly crystalline silicic magma reservoirs (Bachman and
647 Bergantz, 2006; Burgisser and Bergantz, 2011; Huber et al., 2011). As shown schematically in
648 Figure 14, in a first step, the highly crystallized crystal mush has a rigid behavior allowing the
649 circulation and upward migration of fluids exsolved from mafic to intermediate magmas
650 recharge below the silicic crystal mush and which subsequently formed the porphyry-type veins
651 in the shallow part of the system (step 2 in Fig. 14). This scenario is supported by the chemical
652 composition of the silicate melt and fluid inclusions found in the high-temperature (> 600ºC)
653 porphyry veins of Cerro de Pasco and coherent with mechanisms proposed for other porphyry
654 systems (Buret et al., 2016; Tapster et al., 2016). Subsequently (step 3 in Fig. 14), the
655 progressive reheating provided by the circulation of hydrothermal fluids and by the intermediate
656 magma recharges triggered a crystallinity degree decrease of the crystal mush and make it
657 eruptible (Fig. 14). The moderate volume of the volcanic and sub-volcanic rocks present at
658 Cerro de Pasco suggests that, at each step, only a small part of the crystal mush is rejuvenated
659 by localized intermediate magmatic recharges and hydrothermal fluid circulation.
660 The new geochronological data reveal alternating formation of porphyry-type
661 mineralization and volcanic to sub-volcanic bodies emplacements. This is ultimately caused by
662 the physical behavior of the underlying highly crystalline silicic magmatic body. Successive
663 magma recharges and associated fluid exsolution events triggered several episodes of
664 rejuvenation of the crystal mush and of eruptive events. The fact that the PM3 porphyry-type
665 mineralization has been formed in a time span of less than 90 kyr before the emplacement of
666 the quartz-monzonite dykes indicates that crystal mush rejuvenation could be as fast as <100
667 kyr.

Conclusions

The obtained U-Pb and Re-Os ages combined with field observations and previous geochronological data offer a new comprehension of the evolution of the magmatic-hydrothermal system of Cerro de Pasco. A period, at least 400 ka long, including three porphyry mineralization events preceded (by 0.9 Ma or less) the formation of the large epithermal polymetallic deposit of Cerro de Pasco. Further, the results indicate that the three porphyry-type mineralization events alternated with volcanic to sub-volcanic activity.

The study of the SMIs hosted in magmatic quartz from the different volcanic and sub-volcanic rocks suggests that the magma prior to emplacement was stored in an upper-crustal reservoir that was highly crystalline (> 50 %) and in a non-eruptible state, close to the solidus at temperatures as low as 680°C. Several rejuvenation events of this upper crustal reservoir were necessary to form the different volcanic and sub-volcanic rocks. Porphyry mineralization events temporally preceded each episode of subsurface magmatic activity. The silicate melt inclusions hosted in hydrothermal quartz from the different porphyry mineralization events provide information on the dynamics of the magmatic-hydrothermal system. The highly evolved composition of these SMIs suggests that the hydrothermal fluids have circulated through a highly crystalline reservoir in which the residual interstitial melt was strongly evolved too. The primitive fluid inclusions found in PM1 porphyry veins are CO_2- and S-rich, suggesting that the fluid was sourced from an intermediate magmas. All the data are compatible with a model where punctual recharge of intermediate magma crystallized at the contact with the upper-crustal silicic reservoir. In this model, these intermediate magmas during their cooling exsolved CO_2- and S-rich fluids that have circulated through the upper-crustal reservoir and have subsequently formed porphyry-type mineralization. Finally, the thermal energy provided by the intermediate magma itself and by the circulation of the fluids permitted the rejuvenation of parts of the upper-crustal magma reservoir and the formation of the volcanic to sub-volcanic

693 rocks. The high precision CA-ID-TIMS geochronology indicates that these episodes of
694 rejuvenation and porphyry-type mineralization are as short as 90 ka.

695 Acknowledgements

696 This study was supported by the Swiss National Science Foundation (project FN
697 200020_134872). We thank Volcan Compañía Minera S.A. for providing financial and
698 logistical support. Special thanks to the Cerro de Pasco and Volcan Geology staff, in particular
699 to Hugo Alvarez, David Cuellar, César Farfán and Ronner Bendezú. We gratefully
700 acknowledge Jean-Marie Boccard and Fabio Capponi for their help with sample preparation.
701 Early discussions with Vincent Casanova and Cyril Chelle-Michou helped to improve this
702 paper. We are grateful to Simon Large and an anonymous reviewer for their constructive
703 comments which significantly improved the manuscript.

704 References

705 Angeles, C., 1999. Los sedimentos cenozóicos de Cerro de Pasco: Estratigrafía, sedimentación
706 y tectónica. In Macharé, J., Benavides-Caceres, V., and Rosas, S., eds., Sociedad Geológica
707 del Perú SP 5, 103–118.

708 Audétat, A., Pettke, T., 2003. The magmatic-hydrothermal evolution of two barren granites: a
709 melt and fluid inclusion study of the Rito del Medio and Canada Pinabete plutons in northern
710 New Mexico (USA). Geochimica et Cosmochimica Acta 67,97-121.

711 Audétat, A., 2015. Compositional evolution and formation conditions of magmas and fluids
712 related to porphyry Mo mineralization at Climax, Colorado. Journal of Petrology 56, 1519-
713 1546.

714 Audétat, A., Zhang, L., Ni, H., 2018. Copper and Li diffusion in plagioclase, pyroxenes, olivine
715 and apatite, and consequences for the composition of melt inclusions. Geochimica et
716 Cosmochimica Acta 243, 99-115.

717 Audétat, A., 2019. The Metal Content of Magmatic-Hydrothermal Fluids and Its Relationship
718 to Mineralization Potential. Economic Geology 114, 1033-1056.

719 Bachmann, O., Dungan, M.A., Bussy, F., 2005. Insights into shallow magmatic processes in
720 large silicic magmabodies: the trace element record in the Fish Canyon magma body,
721 Colorado. Contribution to Mineralogy and Petrology 149, 338-349.

722 Bachmann, O., Bergantz, G.W., 2006 Gas percolation in upper-crustal silicic crystal mushes as
723 a mechanism for upward heat advection and rejuvenation of near-solidus magma bodies.
724 Journal of Volcanology and Geothermal Research149, 85-102.

725 Bachmann, O., Huber, C., 2016. Silicic magma reservoirs in the Earth's crust. American
726 Mineralogist, 101, 2377-2404.

727 Baumgartner, R., 2007. Sources and evolution in space and time of hydrothermal fluids at the
728 Cerro de Pasco Cordilleran base metal deposit, Central Peru. Terre & Environnement 66,
729 167 p.

730 Baumgartner, R., Fontboté, L., Vennemann, T., 2008. Mineral zoning and geochemistry of
731 epithermal polymetallic Zn-Pb-Ag-Cu-Bi mineralization at Cerro de Pasco, Peru. Economic
732 Geology 103, 493–537.

733 Baumgartner, R., Fontboté, L., Spikings, R., Ovtcharova, M., Schneider, J., Pace, L., Gutjahr,
734 M., 2009. Bracketing the age of magmatic-hydrothermal activity at the Cerro de Pasco
735 epithermal polymetallic deposit, central Peru: a U-Pb and $^{40}Ar/^{39}Ar$ study. Economic
736 Geology 104, 479-504.

737 Black, L.P., Kamo, S.L., Allen, C.M., Davis, D.W., Aleinikoff, J.N., Valley, J.W., et al. 2004.
738 Improved $^{206}Pb/^{23}8U$ microprobe geochronology by the monitoring of a trace-element-
739 related matrix effect; SHRIMP, ID–TIMS, ELA–ICP–MS and oxygen isotope
740 documentation for a series of zircon standards. Chemical Geology 205, 115–140.

741 Bendezú, R., Fontboté, L., 2009. Cordilleran epithermal Cu-Zn-Pb-(Au-Ag) mineralization in
742 the Colquijirca district, Central Peru: Deposit-scale mineralogical patterns: Economic
743 Geology 104, 905–944.

744 Bissig, T., Ullrich, T.D., Tosdal, R.M., Friedman, R., Ebert, S., 2008. The time-space
745 distribution of Eocene to Miocene magmatism in the central Peruvian polymetallic province
746 and its metallogenetic implications. Journal of South American Earth Sciences 26, 16–35.

747 Borisova, A.Y., Freydier, R., Polvé, M., Salvi, S., Candaulap, F., Aigouy, T., 2008. In Situ
748 Multi-Element Analysis of the Mount Pinatubo Quartz-Hosted Melt Inclusions by NIR
749 Femtosecond Laser Ablation-Inductively Coupled Plasma-Mass Spectrometry.
750 Geostandards and Geoanalytical Research 32, 209-229..

751 Buret, Y., Von Quadt, A., Heinrich, C., Selby, D., Wälle, M., Peytcheva, I., 2016. From a long-
752 lived upper-crustal magma chamber to rapid porphyry copper emplacement: Reading the
753 geochemistry of zircon crystals at Bajo de la Alumbrera (NW Argentina). Earth and
754 Planetary Science Letters 450, 120-131.

755 Buret, Y., Wotzlaw, J.F., Roozen, S., Guillong, M., von Quadt, A., Heinrich, C.A., 2017. Zircon
756 petrochronological evidence for a plutonic-volcanic connection in porphyry copper deposits.
757 Geology, G38994-1.

758 Burgisser, A., Bergantz, G.W., 2011, A rapid mechanism to remobilize and homogenize highly
759 crystalline magma bodies. Nature 471, 212–215.

760 Carrichi, L., Blundy, J., 2015. Experimental petrology of monotonous intermediate magmas.
761 In: Chemical, Physical and Temporal Evolution of Magmatic Systems. Geological Society,
762 London, Special Publications 422, 105-130

763 Cashman, K.V., Blundy, J.D., 2013. Petrological cannibalism – the chemical and textural
764 consequences of incremental magma body growth. Contribution to Mineralogy and
765 Petrology 166, 703–729.

766 Cashman, K.V., Sparks, R.S.J., Blundy, J.D., 2017. Vertically extensive and unstable magmatic
767 systems: A unified view of igneous processes. Science 355, eaag3055.

768 Catchpole, H., Kouzmanov, K., Putlitz, B., Seo, J., Fontboté, L., 2015a. Zoned Base Metal
769 Mineralization in a Porphyry System: Origin and Evolution of Mineralizing Fluids in the
770 Morococha District, Peru. Economic Geology 110, 39–71.

771 Catchpole, H., Kouzmanov, K., Bendezú, A., Ovtcharova, M., Spikings, R., Stein, H., Fontboté,
772 L., 2015b. Timing of porphyry (Cu-Mo) and base metal (Zn-Pb-Ag-Cu) mineralisation in a
773 magmatic-hydrothermal system—Morococha district, Peru. Mineralium Deposita, 50, 895-
774 922.

775 Chelle-Michou, C., Rottier, B., Caricchi, L., Simpson, G., 2017. Tempo of magma degassing
776 and the genesis of porphyry copper deposits. Scientific Report 7, 40566.

777 Claiborne, L.L., Miller, C.F., Flanagan, D.M., Clynne, M.A., Wooden, J.L., 2010. Zircon
778 reveals protracted magma storage and recycling beneath Mount St. Helens. Geology, 38,
779 1011-1014.

780 Cooper, K.M., Kent, A.J.R., 2014. Rapid remobilization of magmatic crystals kept in cold
781 storage. Nature 506, 480–483

782 Cooper, K.M., 2017. What Does a Magma Reservoir Look Like? The “Crystal's-Eye” View.
783 Elements 13, 23-28.

784 Deering, C.D., Keller, B., Schoene, B., Bachmann, O., Beane, R., Ovtcharova, M., 2016. Zircon
785 record of the plutonic-volcanic connection and protracted rhyolite melt evolution. Geology
786 44, 267-270.

787 Einaudi, M.T., 1968. Pyrrhotite-pyrite-sphalerite relations at Cerro de Pasco, Peru. Unpublished
788 Ph.D. thesis, Cambridge, MA, Harvard University, 381 p.

789 Ferry, J.M., Watson, E.B., 2007. New thermodynamic models and revised calibrations for the
790 Ti-in-zircon and Zr-in-rutile thermometers. Contribution to Mineralogy and Petrology 154,
791 429–437.

792 Fu, B., Page, F.Z., Cavosie, A.J., Fournelle, J., Kita, N.T., Lackey, J.S., Valley, J.W., 2008. Ti-
793 in-zircon thermometry: Applications and limitations. Contribution to Mineralogy and
794 Petrology 156, 197–215.

795 Guillong M, Meier DL, Allan MM, Heinrich CA, Yardley BWD (2008) SILLS: a Matlab-based
796 program for the reduction of Laser Ablation ICP-MS data of homogeneous materials and
797 inclusions. In: Sylvester, P. (Ed.), Laser-ablation-ICPMS in the earth sciences: current
798 practices and outstanding issues. Mineralogical Association of Canada, Vancouver, B.C.,
799 pp. 328–333.

800 Gutscher, M.A., Olivet, J.L., Aslanian, D., Eissen, J.P., Maury, R., 1999. The “lost Inca
801 Plateau’’: Cause of flat subduction beneath Peru? Earth and Planetary Science Letters 171,
802 335–341.

803 Halter, W.E., Pettke, T., Heinrich, C.A., Roten-Rutishauser, B., 2002. Major to trace element
804 analysis of melt inclusions by laser-ablation ICP-MS: methods of quantification. Chemical
805 Geology 183, 63-86.

806 Halter, W.E., Heinrich, C.A., Pettke, T., 2004. Laser-ablation ICP-MS analysis of sili-cate and
807 sulfide melt inclusions in an andesitic complex II: evidence for magma mixing and magma
808 chamber evolution. Contribution to Mineralogy and Petrology 147, 397–412.

809 Hampel, A., 2002. The migration history of the Nazca Ridge along the Peruvian active margin:
810 a re-evaluation. Earth and Planetary Science Letters 203, 665–679.

811 Hattori, K.H., Keith, J., 2001. Contribution of mafic melt to porphyry copper mineralization:
812 Evidence from Mount Pinatubo, Philippines, and Bingham Canyon, Utah, USA. Mineraliun
813 Deposita 36, 799–806.

814 Huang, R., Audetat, A., 2012. The titanium-in-quartz (TitaniQ) thermobarometer: a critical
815 examination and re-calibration. Geochimica et Cosmochimica Acta 84, 75–89.

816 Huber, C., Bachmann, O., Manga, M., 2010. Two competing effects of volatiles on heat transfer
817 in crystal-rich magmas: Thermal insulation vs. defrosting. Journal of Petrology 51, 847–867.

818 Huber, C., Bachmann, O., Dufek, J., 2011. Thermo-mechanical reactivation of locked crystal
819 mushes: Melting-induced internal fracturation and assimilation processes in magmas. Earth
820 and Planetary Science Letters 304, 443–454.

821 Johnson, E.R., Kamenetsky, V.S., McPhie, J., 2013. The Behavior of Metals (Pb, Zn, As, Mo,
822 Cu) During Crystallization and Degassing of Rhyolites from the Okataina Volcanic Center,
823 Taupo Volcanic Zone, New Zealand. Journal of Petrology 54, 1641-1659.

824 Keller, C. B., Schoene, B., & Samperton, K. M. 2018. A stochastic sampling approach to zircon
825 eruption age interpretation. Geochemical Perspectives Letters, 8, 31-35.

826 Kent, A.J., Darr, C., Koleszar, A.M., Salisbury, M.J., Cooper, K.M., 2010. Preferential eruption
827 of andesitic magmas through recharge filtering. Nature Geoscience 3, 631.

828 Large, S.J., Quadt, A.V., Wotzlaw, J.F., Guillong, M., Heinrich, C.A., 2018. Magma evolution
829 leading to porphyry Au-Cu mineralization at the Ok Tedi deposit, Papua New Guinea: trace
830 element geochemistry and high-precision geochronology of igneous zircon. Economic
831 Geology, 113, 39-61.

832 Large, S.J., Wotzlaw, J.F., Guillong, M., Quadt, A.V., & Heinrich, C.A. 2020. Resolving the
833 timescales of magmatic and hydrothermal processes associated with porphyry deposit
834 formation using zircon U–Pb petrochronology. Geochronology, 2, 209-230.

835 Lee, C.T.A., Bachmann, O., 2014. How important is the role of crystal fractionation in making
836 intermediate magmas? Insights from Zr and P systematics. Earth and Planetary Science
837 Letters, 393, 266-274.

838 Lerchbaumer, L., Audétat, A., 2012. High Cu concentrations in vapor-type fluid inclusions: An
839 artifact?. Geochimica et Cosmochimica Acta 88, 255-274.

840 Mandeville, C.W., Carey, S., Sigurdsson, H., 1996. Magma mixing, fractional crystallization
841 and volatile degassing during the 1883 eruption of Krakatau volcano, Indonesia. Journal of
842 Volcanology and Geothermal Research 74, 243-274

843 Masterman, G.J., Cooke, D.R., Berry, R.F., Clark, A.H., Archibald, D.A., Mathur, R., Walshe,
844 J.L., Durán, M., 2004. $^{40}Ar/^{39}Ar$ and Re-Os geochronology of porphyry copper-molybdenum
845 deposits and related copper-silver veins in the Collahuasi district, northern Chile. Economic
846 Geology, 99, 673-690.

McLennan, S.M., 2001. Relationships between the trace element composition of sedimentary rocks and upper continental crust. Geochemistry, Geophysics, Geosystems 2, 1021.

Mustard, R., Ulrich, T., Kamenetsky, V.S., Merbagh, T., 2006. Gold and metal enrichment in natural granitic melts during fractional crystallization. Geology 34, 85-88.

Nadeau, O., Stix, J., Williams-Jones, A.E., 2013. The behavior of Cu, Zn and Pb during magmatic–hydrothermal activity at Merapi volcano, Indonesia. Chemical Geology 342, 167-179.

Noble, D.C., McKee, E.H., 1999. The Miocene metallogenic belt of central and northern Peru. Society of Economic Geologists Special Publications 7,155–193.

Papale, P., Moretti, R., Barbato, D., 2006. The compositional dependence of the saturation surface of H_2O+CO_2 fluids in silicate melts. Chemical Geology, 229, 78-95.

Parmigiani, A., Faroughi, S., Huber, C., Bachmann, O., Su, Y., 2016. Bubble accumulation and its role in the evolution of magma reservoirs in the upper crust. Nature, 532, 492-495.

Price, R.C., Gamble, J.A., Smith, I.E.M., Stewart, R.B., Eggins, E., Wright, I.C., 2005. An integrated model for the temporal evolution of andesites and rhyolites and crustal development in New Zealand's North Island. Journal of Volcanology and Geothermal Research 140, 1-24.

Reubi, O., Blundy, J., 2009. A dearth of intermediate melts at subduction zone volcanoes and the petrogenesis of arc andesites. Nature 461, 1269.

Rogers, R., 1983. Structural and geochemical evolution of a mineralized volcanic vent at Cerro de Pasco, Peru: Unpublished PhD thesis, Tucson, University of Arizona, 116 p.

868 Rosas, S., Fontboté, L., Tankard, A., 2007. Tectonic evolution and paleogeography of the
869 Mesozoic Pucará Basin, central Peru: Journal of South American Earth Sciences 26, 16–35.

870 Rosenbaum, G., Giles, D., Saxon, M., Betts, P.G., Weinberg, R.F., Duboz, C., 2005. Subduction
871 of the Nazca Ridge and the Inca Plateau: Insights into the formation of ore deposits in Peru.
872 Earth and Planetary Science Letters 239, 18–32.

873 Rottier, B., 2016. Magmatic and hydrothermal fluid processes at the origin of the giant
874 porphyry-related epithermal polymetallic deposit of Cerro de Pasco (Central Peru), PhD
875 thesis. Univ. Geneva. 431p.

876 Rottier, B., Kouzmanov, K., Bouvier, A.S., Baumgartner, L., Wälle, M., Rezeau, H., Bendezú,
877 R., Fontboté, L., 2016a. Heterogeneous melt and hypersaline liquid inclusions in shallow
878 porphyry type mineralization as markers of the magmatic-hydrothermal transition (Cerro
879 de Pasco district, Peru). Chemical Geology 447, 93-116.

880 Rottier. B., Kouzmanov, K., Wälle, M., Bendezú, R., Fontboté, L., 2016b. Sulfide replacement
881 processes revealed by textural an LA-ICP-MS trace element analyses: example from the
882 early mineralization stages at Cerro de Pasco, Peru. Economic Geology 111, 1347-1367.

883 Rottier, B., Rezeau, H., Casanova, V., Kouzmanov, K., Moritz, R., Schlöglova, K., Wälle, M.,
884 Fontboté, L., 2017. Trace element diffusion and incorporation in quartz during heating
885 experiments. Contribution to Mineralogy and Petrology 172, 23.

886 Rottier, B., Kouzmanov, K., Casanova, C., Bouvier, A.S., Baumgartner, L., Wälle, M.,
887 Fontboté, L., 2018a. Mineralized breccia clasts: a window into hidden porphyry-type
888 mineralization underlying the epithermal polymetallic deposit of Cerro de Pasco (Peru).
889 Mineraliun Deposita 53, 919-946.

Rottier. B., Kouzmanov, K., Casanova, V., Wälle, M., Fontboté, L., 2018b. Cyclic dilution of magmatic metal-rich hypersaline fluids by magmatic low-salinity fluid: a major process generating the giant epithermal polymetallic deposit of Cerro de Pasco, Peru. Economic Geology 113, 825-856.

Rottier, B., Audétat, A., Koděra, P., Lexa, J., 2019. Origin and evolution of magmas in the porphyry Au -mineralized Javorie volcano (Central Slovakia): evidence from thermobarometry, melt inclusions, and sulfide inclusions. Journal of Petrology, 60, 2449-2482.

Rottier, B., Audétat, A., Koděra, P., Lexa, J., 2020b. Magmatic evolution of the mineralized Štiavnica volcano (Central Slovakia): evidence from thermobarometry, melt inclusions, and sulfide inclusions. Journal of Volcanology and Geothermal Research, 106967

Schoene, B., Schaltegger, U., Brack, P., Latkoczy, C., Stracke, A., Günther, D., 2012. Rates of magma differentiation and emplacement in a ballooning pluton recorded by U–Pb TIMS-TEA, Adamello batholith, Italy. Earth and Planetary Science Letters 355–356, 162–173.

Sillitoe, R.H., 2010. Porphyry copper systems. Economic Geology 105, 3-41.

Spencer, T.E., Wilkinson, J.J., Creaser, R.A., Seguel, J., 2015. The Distribution and Timing of Molybdenite Mineralization at the El Teniente Cu-Mo Porphyry Deposit, Chile. Economic Geology 110, 387-421.

Spikings, R., Reitsma, M.J., Boekhout, F., Mišković, A., Ulianov, A., Chiaradia, M., Gerdes, A., Schaltegger, U., 2016. Characterization of Triassic rifting in Peru and implications for the early disassembly of western Pangaea: Gondwana Research 35, 124–143.

911 Stefanova, E., Driesner, T., Zajacz, Z., Heinrich, C.A., Petrov, P., Vasilev, Z., 2014. Melt and
912 Fluid Inclusions in Hydrothermal Veins: The Magmatic to Hydrothermal Evolution of the
913 Elatsite Porphyry Cu-Au Deposit, Bulgaria. Economic Geology 109, 1359-1381.

914 Szymanowski, D., Wotzlaw, J.F., Ellis, B.S., Bachmann, O., Guillong, M., von Quadt, A., 2017.
915 Protracted near-solidus storage and pre-eruptive rejuvenation of large magma reservoirs.
916 Nature Geoscience 10, 777-782.

917 Tapster, S., Condon, D.J., Naden, J., Noble, S.R., Petterson, M.G., Roberts, N.M.W., Smith,
918 D.J., 2016. Rapid thermal rejuvenation of high-crystallinity magma linked to porphyry
919 copper deposit formation; evidence from the Koloula Porphyry Prospect, Solomon Islands.
920 Earth and Planetary Science Letters 442, 206-217.

921 Ulianov. A., Müntener, O., Schaltegger, U., Bussy, F., 2012. The data treatment dependent
922 variability of U–Pb zircon ages obtained using mono-collector, sector field, laser ablation
923 ICPMS. Journal of Analytical Atomic Spectrometry 27, 663–676.

924 Watson, E.B., Harrison, T.M., 1983. Zircon saturation revisited: temperature and composition
925 effects in a variety of crustal magma types. Earth and Planetary Science Letters 64, 295-304.

926 Watson, E.B., Wark, D.A., Thomas, J.B., 2006. Crystallization thermometers for zircon and
927 rutile: Contribution to Mineralogy and Petrology 151,413–444.

928 Weber, G., Simpson, G., & Caricchi, L., 2020, Magma diversity reflects recharge regime and
929 thermal structure of the crust. Scientific Report, 10:11867.

930 Wotzlaw, J.F., Schaltegger, U., Frick, D.A., Dungan, M.A., Gerdes, A., Günther, D., 2013.
931 Tracking the evolution of large-volume silicic magma reservoirs from assembly to
932 supereruption. Geology, 41, 867-870.

933 Zajacz, Z., Tsay, A., 2019. An accurate model to predict sulfur concentration at anhydrite
934 saturation in silicate melts. Geochimica et Cosmochimica Acta, 261, 288-304.

935 Zhang, D., Audétat, A., 2017. What caused the formation of the giant Bingham Canyon
936 porphyry Cu-Mo-Au deposit? Insights from melt inclusions and magmatic sulfides.
937 Economic Geology, 112, 221-244.

938 Figure captions:

939 **Figure 1**: Geological map and cross-section of the diatreme dome complex and epithermal
940 mineralization styles at Cerro de Pasco; slightly modified from Rottier et al. (2016b), compiled
941 from field observations and previous work of Rogers (1983), Baumgartner et al. (2008) and the
942 Volcan's geological staff. A) Location of the Cerro de Pasco district; B) Geological map; C)
943 Porphyritic trachyte outcrop affected by porphyry-type mineralization PM2.

944 **Figure 2**: A-C) Magmatic (A) and hornfels (B-C) clasts found in the diatreme breccia crosscut
945 by HT1-type (A and C) and HT2-type, modified from Rottier et al. (2018a) (B) sulfide-poor
946 quartz-molybdenite-(chalcopyrite)-(pyrite) veins belonging to the porphyry-type
947 mineralization PM1. D) Magmatic clast found in a quartz-monzonite dyke and affected by
948 porphyry-type mineralization PM3 (sample CP-14-BR-X1). The clast is affected by pervasive
949 silicification and crosscut by A- and B-type quartz-magnetite-chalcopyrite-pyrite veins with
950 potassic alteration halo. Sample selected for U-Pb zircon dating; E) Sample of the dated
951 porphyritic trachyte intrusion crosscut by quartz-magnetite-chalcopyrite-pyrite veinlets
952 (porphyry-type mineralization PM2).

953 **Figure 3**: A) Chondrite-normalized (Sun and McDonough, 1995) REE pattern for rims and
954 cores of zircon crystals from the mineralized magmatic clast and the mineralized trachyte
955 porphyry. B) Importance of REE Kd of each mineral relative to the bulk REE Kd of the mineral

assemblages constituting the magmatic rock, considering the mineral composition of the trachyte porphyry as determined by the QEMSCAN analysis. C) Trace element signatures of analyzed zircons, Yb/Dy ratio versus Th/U ratio, Ce content and HREE. Core and rim of each analyzed zircon grain are connected with gray lines. Normally zoned (circle) and reversely zoned (diamond) zircons are represented separately (see text). D) SEM-CL image of a reversely zoned zircon from the trachyte porphyry showing dissolution episode between core and rim. The black circles refer to locations of LA-ICP-MS analyses.

Figure 4: Geochronology of the various magmatic events at Cerro de Pasco. (A) LA-ICPMS $^{206}Pb/^{238}U$ ages with weighted mean age and the corresponding probability density plot for each sample. (B) CA-ID-TIMS $^{206}Pb/^{238}U$ ages with weighted mean values of statistically equivalent zircon populations (red vertical bars); previous data published by Baumgartner et al. (2009) are also included for comparison. All uncertainties are reported at the 95% (2σ) confidence level. (C) Re-Os dates for a molybdenite separate (sample CP-16-BR-X4), uncertainty includes all sources of analytical uncertainty and the one related to the decay constant (Smoliar et al., 1996; Begemann et al., 2001).

Figure 5: Mineral composition and texture of volcanic and subvolcanic magmatic rocks from Cerro de Pasco - transmitted light photomicrograph, QEMSCAN mineral maps and QEMSCAN Ca distribution maps (intensity of the green color reflects the Ca-content in plagioclase and yellow color indicates presence of apatite and titanite): A) Dacitic tuff, B) Dacitic lava-dome complex, C) Rhyodacitic lava-dome complex, D) Quartz-monzonite dyke. Quantitative mineralogy of the rocks is based on the area% of each mineral determined from the QEMSCAN maps.

Figure 6: Mineral composition and texture of the porphyritic trachyte - transmitted light photomicrograph, QEMSCAN mineral map and QEMSCAN Ca distribution map (intensity of

980 the green color reflects the Ca-content in plagioclase and yellow color indicates presence of
981 calcite, apatite, titanite and epidote). Chlorite, epidote and calcite result from a low-temperature
982 hydrothermal alteration associated with the quartz-magnetite-chalcopyrite-(pyrite) stockwork.

983 **Figure 7**: (A) Photomicrograph of an apatite crystal with inclusions of magmatic calcite and
984 anhydrite (transmitted light, //N). (B) Raman spectrum of calcite inclusion in apatite. (C) Raman
985 spectrum of anhydrite inclusion in apatite.

986 **Figure 8**: (A) Chondrite-normalized REE patterns (chondrite composition from Sun and
987 McDonough, 1995); (B) Primitive mantle-normalized trace element patterns (chondrite
988 composition from Sun and McDonough 1995). For A and B the red fields correspond to the
989 range of compositions of whole-rock samples from Cerro de Pasco and the gray field - to
990 compositions of Oligocene and Miocene magmatic rocks from the central Peruvian Cordillera
991 Occidental compiled by Bissig and Tosdal (2009); C) Sr/Y vs. Y; D) La/Yb vs. Yb. In C and
992 D, the dashed lines represent the adakite field (all data are in supplementary table A.9).

993 **Figure 9**: Silicate melt inclusions hosted in magmatic and hydrothermal quartz. A) Glassy
994 silicate melt inclusions hosted in magmatic quartz phenocryst from a rhyodacitic dome. B)
995 Glassy silicate melt inclusions hosted in hydrothermal quartz from PM1 quartz–molybdenite–
996 (chalcopyrite)–(pyrite) veins. C) Glassy silicate melt inclusions hosted in hydrothermal quartz
997 from PM3 quartz–magnetite–(chalcopyrite)–(pyrite) veins (mgt: magnetite).

998 **Figure 10**: Major element composition of the whole rock and the silicate melt inclusion. A)
999 Al_2O_3 vs. SiO_2; B) Fe_2O_3 vs. SiO_2; C) MgO vs. SiO_2; D) CaO vs. SiO_2; E) K_2O vs. SiO_2 (all
1000 data are available in supplementary Tables A.9 to A.11).

1001 **Figure 11**: Trace element composition of the whole rocks and SMIs hosted in magmatic and
1002 hydrothermal quartz. A) Rb vs. Cs; B) Sr vs. Cs; C) Zn vs. Cs; D) Cu vs. Cs; E) Pb vs. Cs; F)
1003 W vs. Cs; G) Mo vs. Cs (all data are available in supplementary Tables A.9 to A.11).

Figure 12: Compilation of ID-TIMS U-Pb ages of magmatic rocks obtained in this study and by Baumgartner et al. (2009), the obtained Re-Os ages of molybdenite separate from PM1, the potential age range based on cross-cutting relationships for the hydrothermal events and the $^{40}Ar/^{39}Ar$ ages of alunite attributed to the enargite-pyrite veins (Baumgartner et al., 2009). Modified after Rottier (2017).

Figure 13: A) Median Cs content of volcanic rocks classified by rock types. Hexagons are the median of Oligocene and Miocene magmatic rocks from the central Peruvian Cordillera Occidental compiled by Bissig and Tosdal (2009). B) Distribution of Cs content of the whole rock, the quartz-hosted SMIs from different magmatic rocks (BR-201; BR-235, BR-230; BR-232) and from the porphyry veins of PM1 and PM3. C) Evolution of Cs concentration of the melt versus crystallinity, considering the two constructed model of fractional crystallization in a closed system. The color bars along the X-axis correspond to the crystallinity ranges necessary to reproduce the Cs concentration measured in the quartz-hosted SMIs.

Figure 14: Conceptual model of crystal mush rejuvenation by circulation of MVP exsolved from an underplating andesitic magma.

Figure 1:

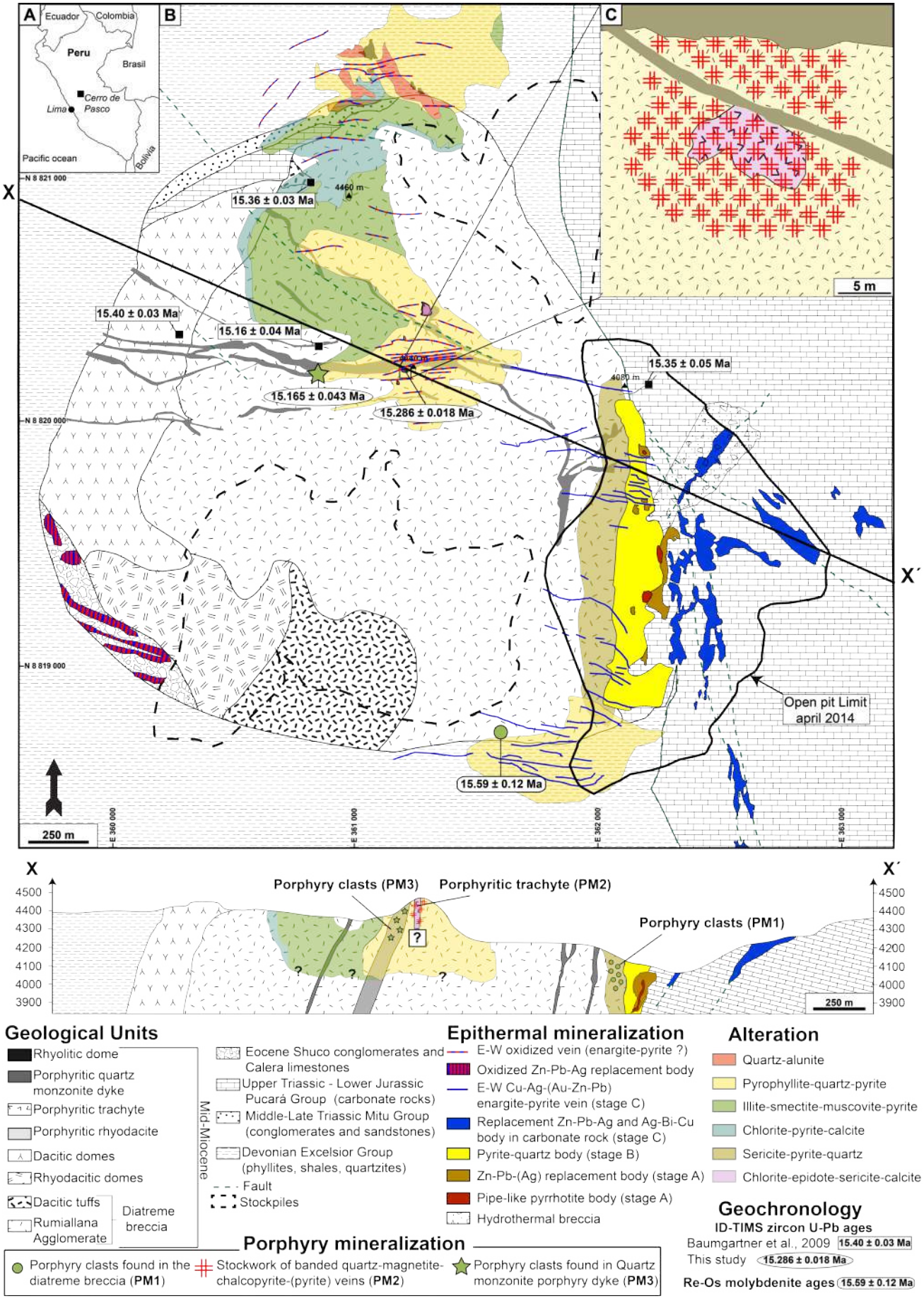
A
Ecuador
Colombia
Peru
Brasil
Cerro de Pasco
Lima
Pacific ocean
Bolivia
B
C
5 m
X
X´
15.36 ± 0.03 Ma
4460 m
15.40 ± 0.03 Ma
15.16 ± 0.04 Ma
15.165 ± 0.043 Ma
15.286 ± 0.018 Ma
15.35 ± 0.05 Ma
4080 m
15.59 ± 0.12 Ma
Open pit Limit april 2014
N 8 821 000
N 8 820 000
N 8 819 000
E 360 000
E 361 000
E 362 000
E 363 000
250 m
Porphyry clasts (PM3)
Porphyritic trachyte (PM2)
Porphyry clasts (PM1)
4500
4400
4300
4200
4100
4000
3900
Geological Units
Rhyolitic dome
Porphyritic quartz monzonite dyke
Porphyritic trachyte
Porphyritic rhyodacite
Dacitic domes
Rhyodacitic domes
Dacitic tuffs
Rumiallana Agglomerate
Diatreme breccia
Mid-Miocene
Eocene Shuco conglomerates and Calera limestones
Upper Triassic - Lower Jurassic Pucará Group (carbonate rocks)
Middle-Late Triassic Mitu Group (conglomerates and sandstones)
Devonian Excelsior Group (phyllites, shales, quartzites)
Fault
Stockpiles
Epithermal mineralization
E-W oxidized vein (enargite-pyrite ?)
Oxidized Zn-Pb-Ag replacement body
E-W Cu-Ag-(Au-Zn-Pb) enargite-pyrite vein (stage C)
Replacement Zn-Pb-Ag and Ag-Bi-Cu body in carbonate rock (stage C)
Pyrite-quartz body (stage B)
Zn-Pb-(Ag) replacement body (stage A)
Pipe-like pyrrhotite body (stage A)
Hydrothermal breccia
Alteration
Quartz-alunite
Pyrophyllite-quartz-pyrite
Illite-smectite-muscovite-pyrite
Chlorite-pyrite-calcite
Sericite-pyrite-quartz
Chlorite-epidote-sericite-calcite
Geochronology
ID-TIMS zircon U-Pb ages
Baumgartner et al., 2009 15.40 ± 0.03 Ma
This study 15.286 ± 0.018 Ma
Re-Os molybdenite ages 15.59 ± 0.12 Ma
Porphyry mineralization
Porphyry clasts found in the diatreme breccia (PM1)
Stockwork of banded quartz-magnetite-chalcopyrite-(pyrite) veins (PM2)
Porphyry clasts found in Quartz monzonite porphyry dyke (PM3)

Figure 2:

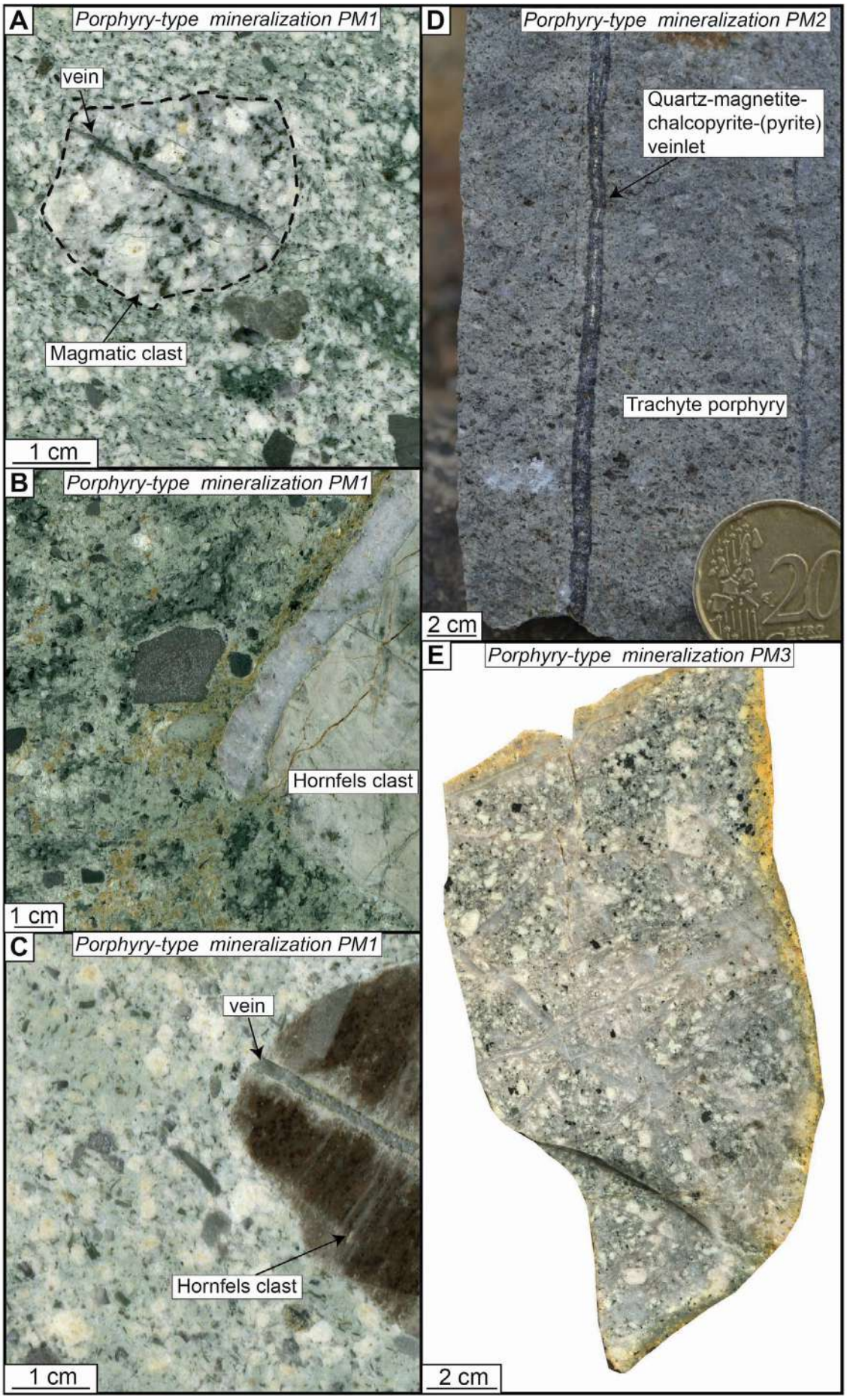
A
Porphyry-type mineralization PM1
vein
Magmatic clast
1 cm
B
Porphyry-type mineralization PM1
Hornfels clast
1 cm
C
Porphyry-type mineralization PM1
vein
Hornfels clast
1 cm
D
Porphyry-type mineralization PM2
Quartz-magnetite-chalcopyrite-(pyrite) veinlet
Trachyte porphyry
2 cm
E
Porphyry-type mineralization PM3
2 cm

Figure 3:

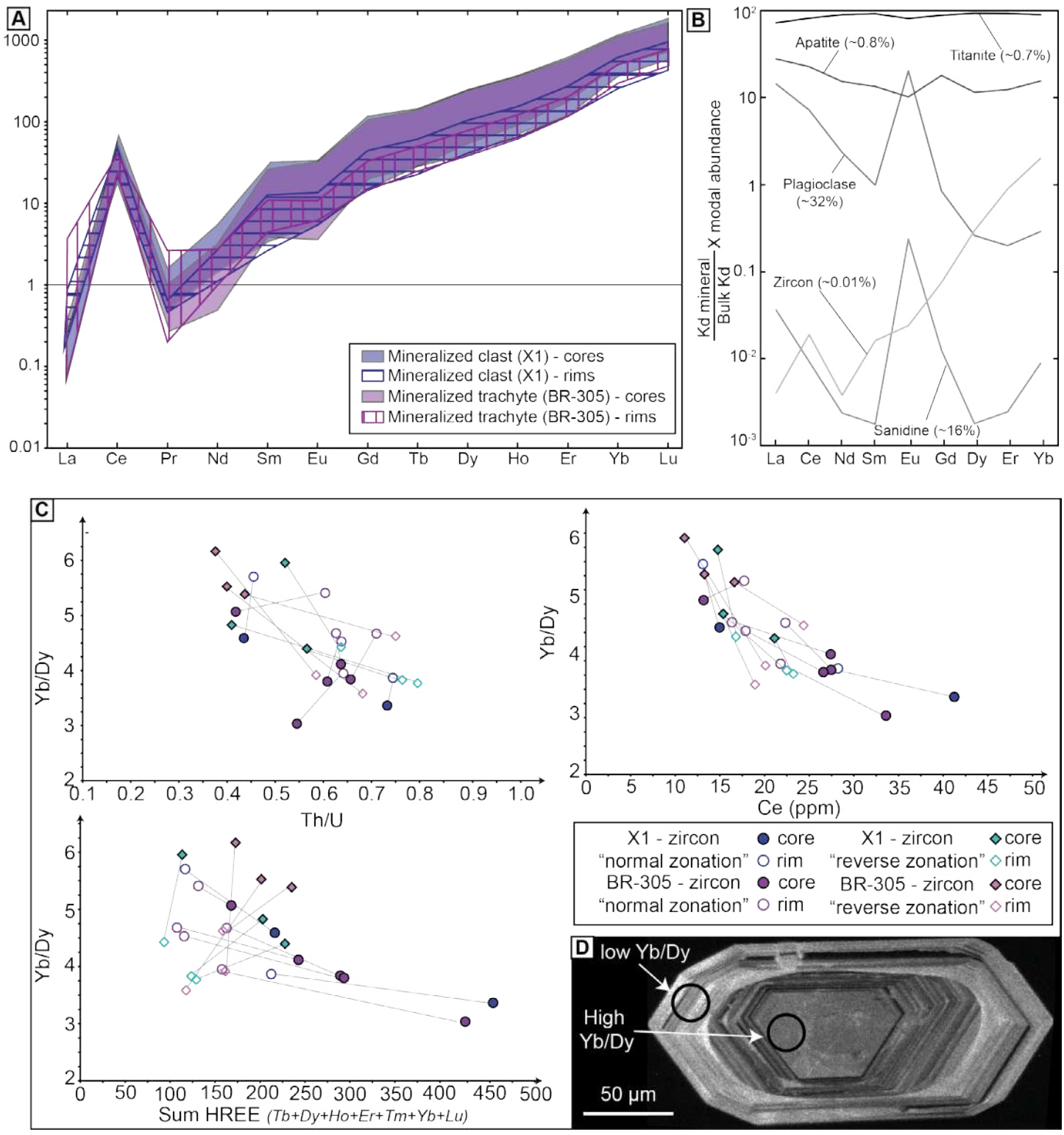
A
1000
100
10
1
0.1
0.01
La Ce Pr Nd Sm Eu Gd Tb Dy Ho Er Yb Lu
Mineralized clast (X1) - cores
Mineralized clast (X1) - rims
Mineralized trachyte (BR-305) - cores
Mineralized trachyte (BR-305) - rims
B
Apatite (~0.8%)
Titanite (~0.7%)
Plagioclase (~32%)
Zircon (~0.01%)
Sanidine (~16%)
Kd mineral / Bulk Kd X modal abundance
La Ce Nd Sm Eu Gd Dy Er Yb
C
Yb/Dy
Th/U
Ce (ppm)
Sum HREE (Tb+Dy+Ho+Er+Tm+Yb+Lu)
X1 - zircon "normal zonation" core rim
X1 - zircon "reverse zonation" core rim
BR-305 - zircon "normal zonation" core rim
BR-305 - zircon "reverse zonation" core rim
D
low Yb/Dy
High Yb/Dy
50 µm

Figure 4:

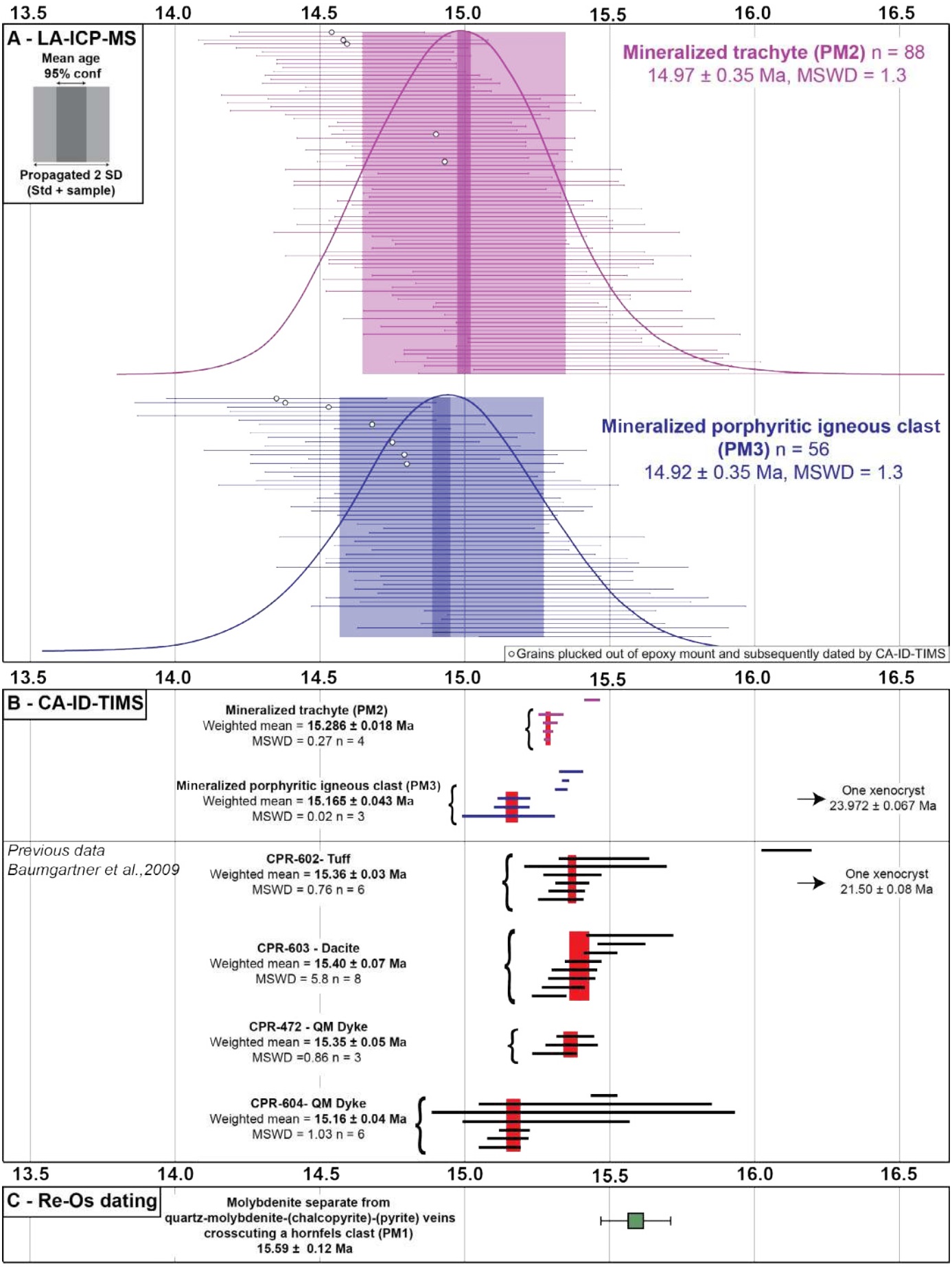
13.5
14.0
14.5
15.0
15.5
16.0
16.5
A - LA-ICP-MS
Mean age
95% conf
Propagated 2 SD
(Std + sample)
Mineralized trachyte (PM2) n = 88
14.97 ± 0.35 Ma, MSWD = 1.3
Mineralized porphyritic igneous clast
(PM3) n = 56
14.92 ± 0.35 Ma, MSWD = 1.3
Grains plucked out of epoxy mount and subsequently dated by CA-ID-TIMS
B - CA-ID-TIMS
Mineralized trachyte (PM2)
Weighted mean = 15.286 ± 0.018 Ma
MSWD = 0.27 n = 4
Mineralized porphyritic igneous clast (PM3)
Weighted mean = 15.165 ± 0.043 Ma
MSWD = 0.02 n = 3
One xenocryst
23.972 ± 0.067 Ma
Previous data
Baumgartner et al.,2009
CPR-602- Tuff
Weighted mean = 15.36 ± 0.03 Ma
MSWD = 0.76 n = 6
One xenocryst
21.50 ± 0.08 Ma
CPR-603 - Dacite
Weighted mean = 15.40 ± 0.07 Ma
MSWD = 5.8 n = 8
CPR-472 - QM Dyke
Weighted mean = 15.35 ± 0.05 Ma
MSWD =0.86 n = 3
CPR-604- QM Dyke
Weighted mean = 15.16 ± 0.04 Ma
MSWD = 1.03 n = 6
C - Re-Os dating
Molybdenite separate from
quartz-molybdenite-(chalcopyrite)-(pyrite) veins
crosscuting a hornfels clast (PM1)
15.59 ± 0.12 Ma

Figure 5:

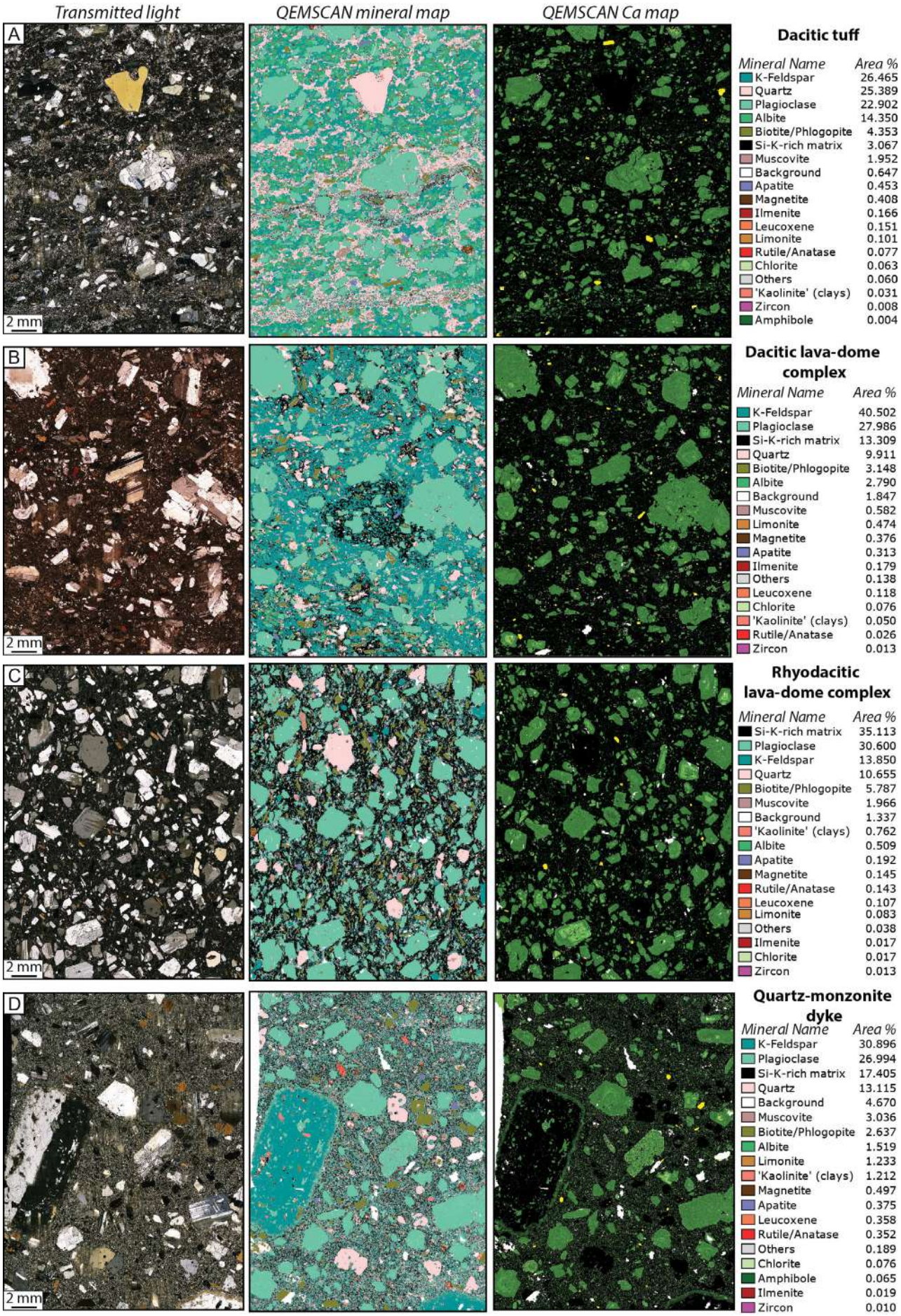
Transmitted light
QEMSCAN mineral map
QEMSCAN Ca map
A
2 mm
B
2 mm
C
2 mm
D
2 mm
Dacitic tuff
Mineral Name Area %
K-Feldspar 26.465
Quartz 25.389
Plagioclase 22.902
Albite 14.350
Biotite/Phlogopite 4.353
Si-K-rich matrix 3.067
Muscovite 1.952
Background 0.647
Apatite 0.453
Magnetite 0.408
Ilmenite 0.166
Leucoxene 0.151
Limonite 0.101
Rutile/Anatase 0.077
Chlorite 0.063
Others 0.060
'Kaolinite' (clays) 0.031
Zircon 0.008
Amphibole 0.004
Dacitic lava-dome complex
Mineral Name Area %
K-Feldspar 40.502
Plagioclase 27.986
Si-K-rich matrix 13.309
Quartz 9.911
Biotite/Phlogopite 3.148
Albite 2.790
Background 1.847
Muscovite 0.582
Limonite 0.474
Magnetite 0.376
Apatite 0.313
Ilmenite 0.179
Others 0.138
Leucoxene 0.118
Chlorite 0.076
'Kaolinite' (clays) 0.050
Rutile/Anatase 0.026
Zircon 0.013
Rhyodacitic lava-dome complex
Mineral Name Area %
Si-K-rich matrix 35.113
Plagioclase 30.600
K-Feldspar 13.850
Quartz 10.655
Biotite/Phlogopite 5.787
Muscovite 1.966
Background 1.337
'Kaolinite' (clays) 0.762
Albite 0.509
Apatite 0.192
Magnetite 0.145
Rutile/Anatase 0.143
Leucoxene 0.107
Limonite 0.083
Others 0.038
Ilmenite 0.017
Chlorite 0.017
Zircon 0.013
Quartz-monzonite dyke
Mineral Name Area %
K-Feldspar 30.896
Plagioclase 26.994
Si-K-rich matrix 17.405
Quartz 13.115
Background 4.670
Muscovite 3.036
Biotite/Phlogopite 2.637
Albite 1.519
Limonite 1.233
'Kaolinite' (clays) 1.212
Magnetite 0.497
Apatite 0.375
Leucoxene 0.358
Rutile/Anatase 0.352
Others 0.189
Chlorite 0.076
Amphibole 0.065
Ilmenite 0.019
Zircon 0.010

Figure 6:

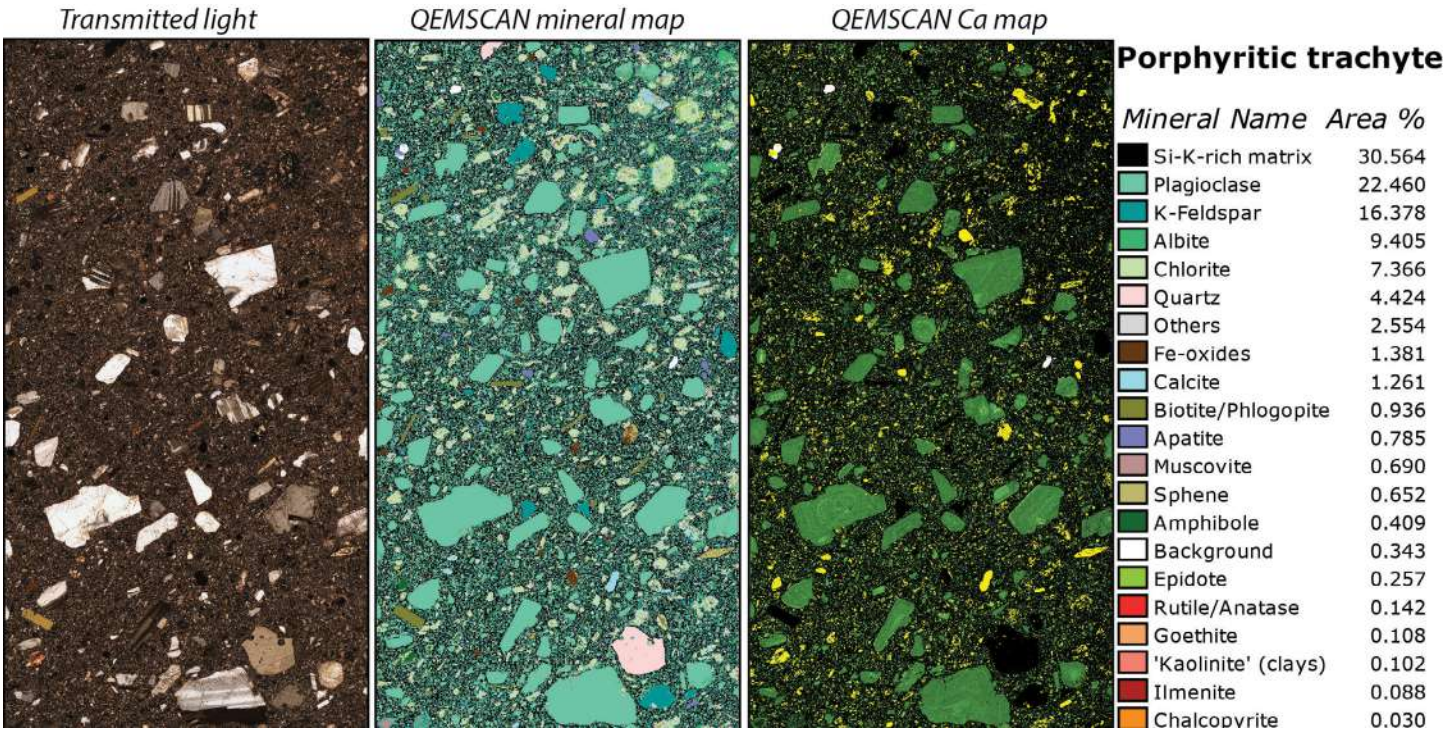
Transmitted light
QEMSCAN mineral map
QEMSCAN Ca map
Porphyritic trachyte
Mineral Name Area %
Si-K-rich matrix 30.564
Plagioclase 22.460
K-Feldspar 16.378
Albite 9.405
Chlorite 7.366
Quartz 4.424
Others 2.554
Fe-oxides 1.381
Calcite 1.261
Biotite/Phlogopite 0.936
Apatite 0.785
Muscovite 0.690
Sphene 0.652
Amphibole 0.409
Background 0.343
Epidote 0.257
Rutile/Anatase 0.142
Goethite 0.108
'Kaolinite' (clays) 0.102
Ilmenite 0.088
Chalcopyrite 0.030

Figure 7:

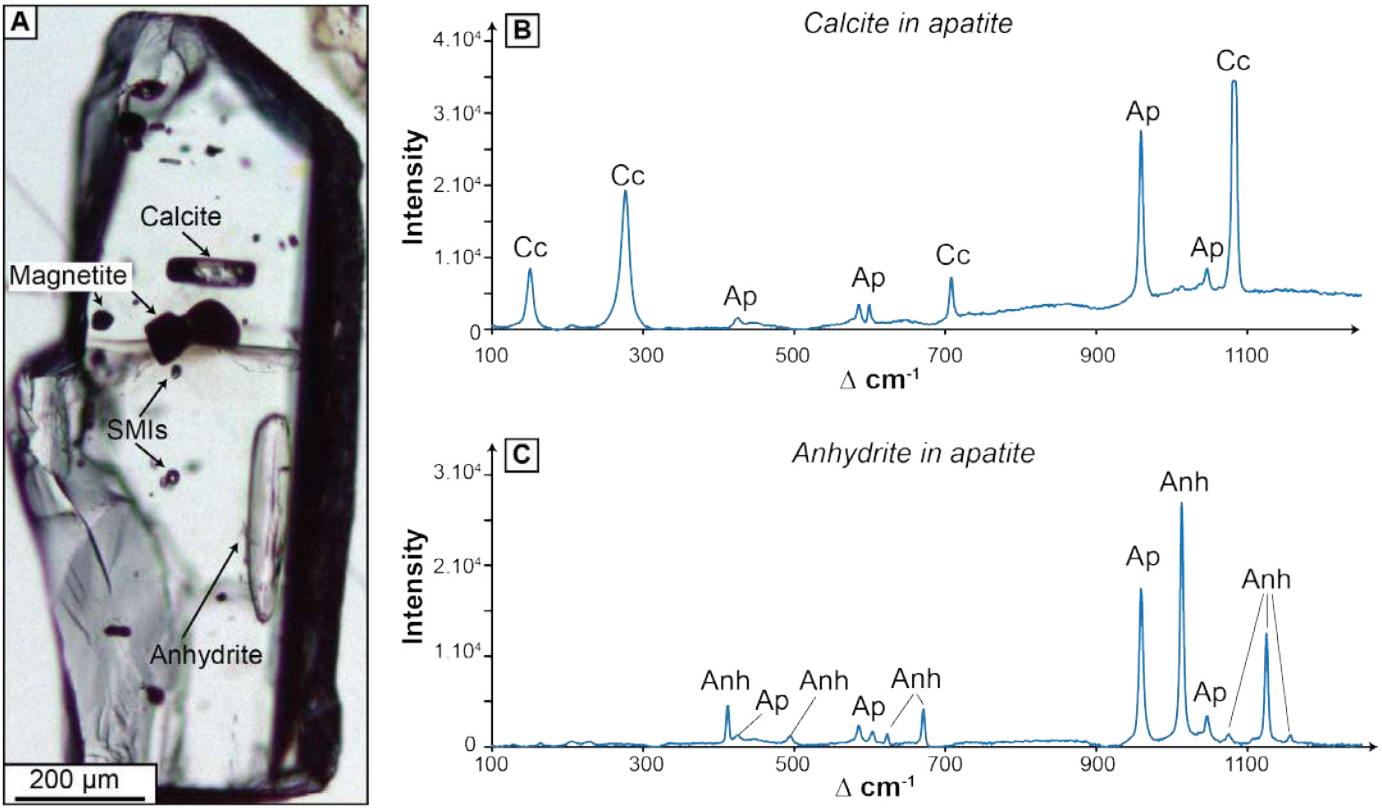
A
Calcite
Magnetite
SMIs
Anhydrite
200 µm
B
Calcite in apatite
Intensity
4.10⁴
3.10⁴
2.10⁴
1.10⁴
0
Cc
Cc
Ap
Ap
Cc
Ap
Ap
Cc
100
300
500
700
900
1100
Δ cm⁻¹
C
Anhydrite in apatite
Intensity
3.10⁴
2.10⁴
1.10⁴
0
Anh
Ap
Anh
Ap
Anh
Ap
Anh
Ap
Anh
100
300
500
700
900
1100
Δ cm⁻¹

Figure 8:

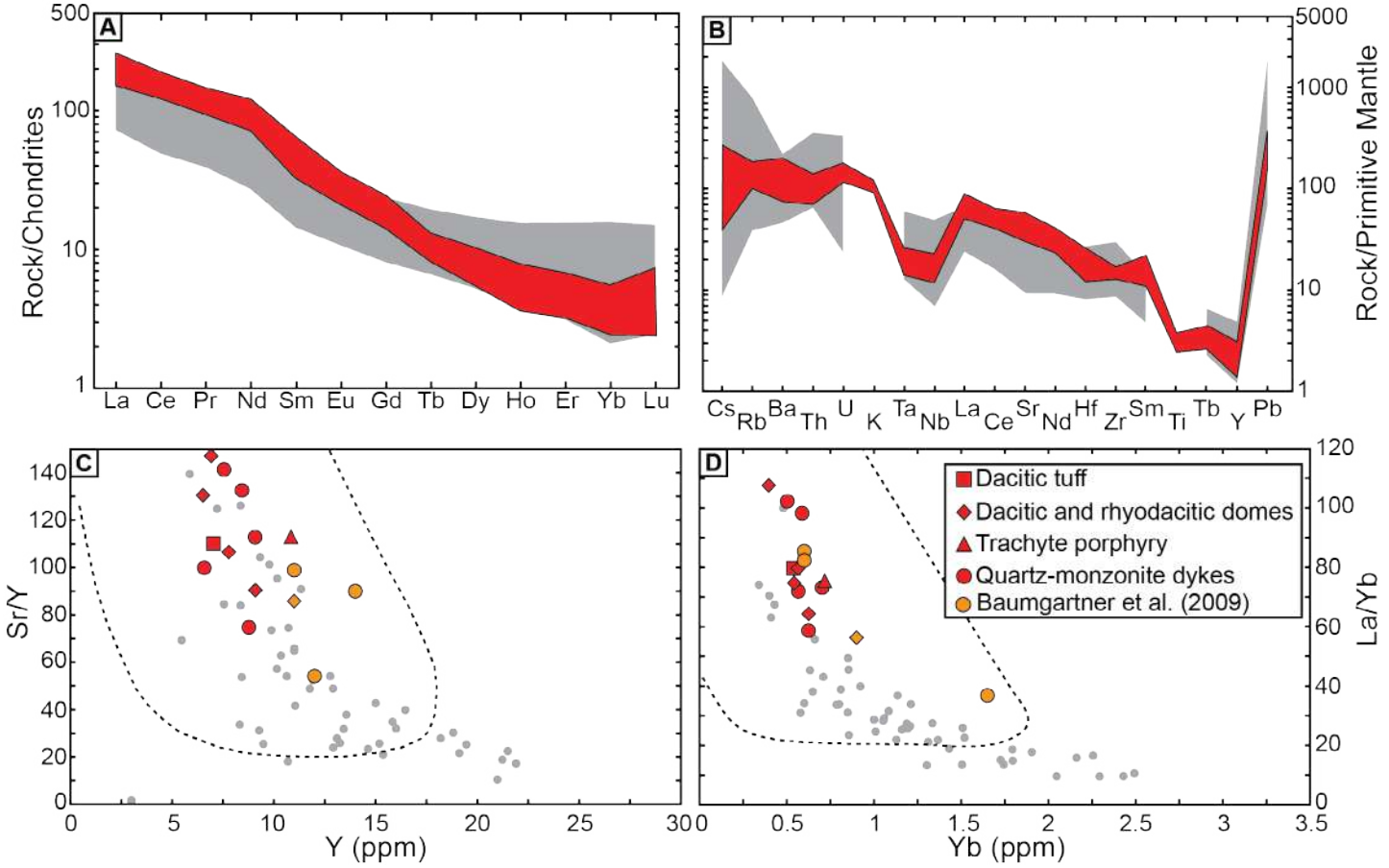
A
Rock/Chondrites
500
100
10
1
La Ce Pr Nd Sm Eu Gd Tb Dy Ho Er Yb Lu
B
Rock/Primitive Mantle
5000
1000
100
10
1
Cs Rb Ba Th U K Ta Nb La Ce Sr Nd Hf Zr Sm Ti Tb Y Pb
C
Sr/Y
140
120
100
80
60
40
20
0
0 5 10 15 20 25 30
Y (ppm)
D
La/Yb
120
100
80
60
40
20
0
0 0.5 1 1.5 2 2.5 3 3.5
Yb (ppm)
Dacitic tuff
Dacitic and rhyodacitic domes
Trachyte porphyry
Quartz-monzonite dykes
Baumgartner et al. (2009)

Figure 9:

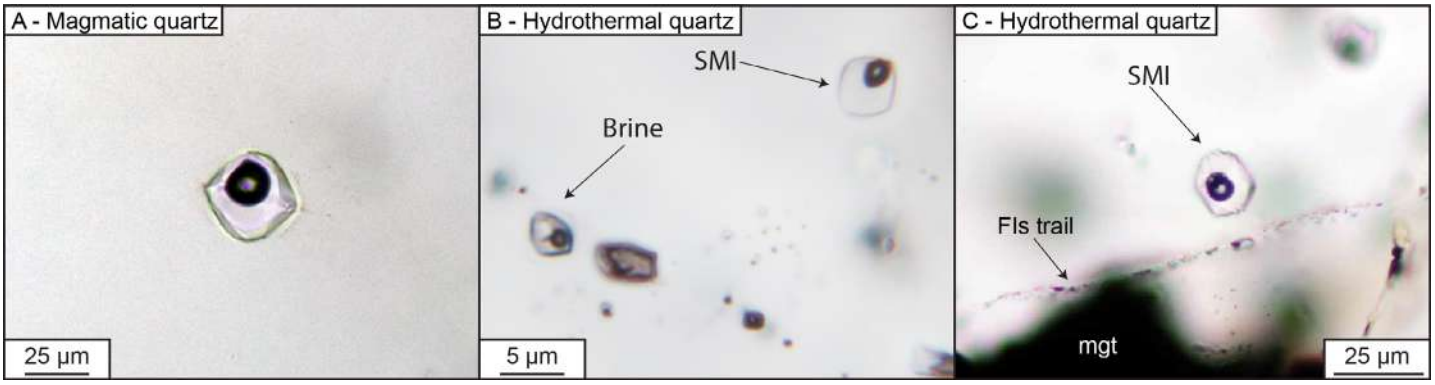
A - Magmatic quartz
25 µm
B - Hydrothermal quartz
SMI
Brine
5 µm
C - Hydrothermal quartz
SMI
FIs trail
mgt
25 µm

Figure 10:

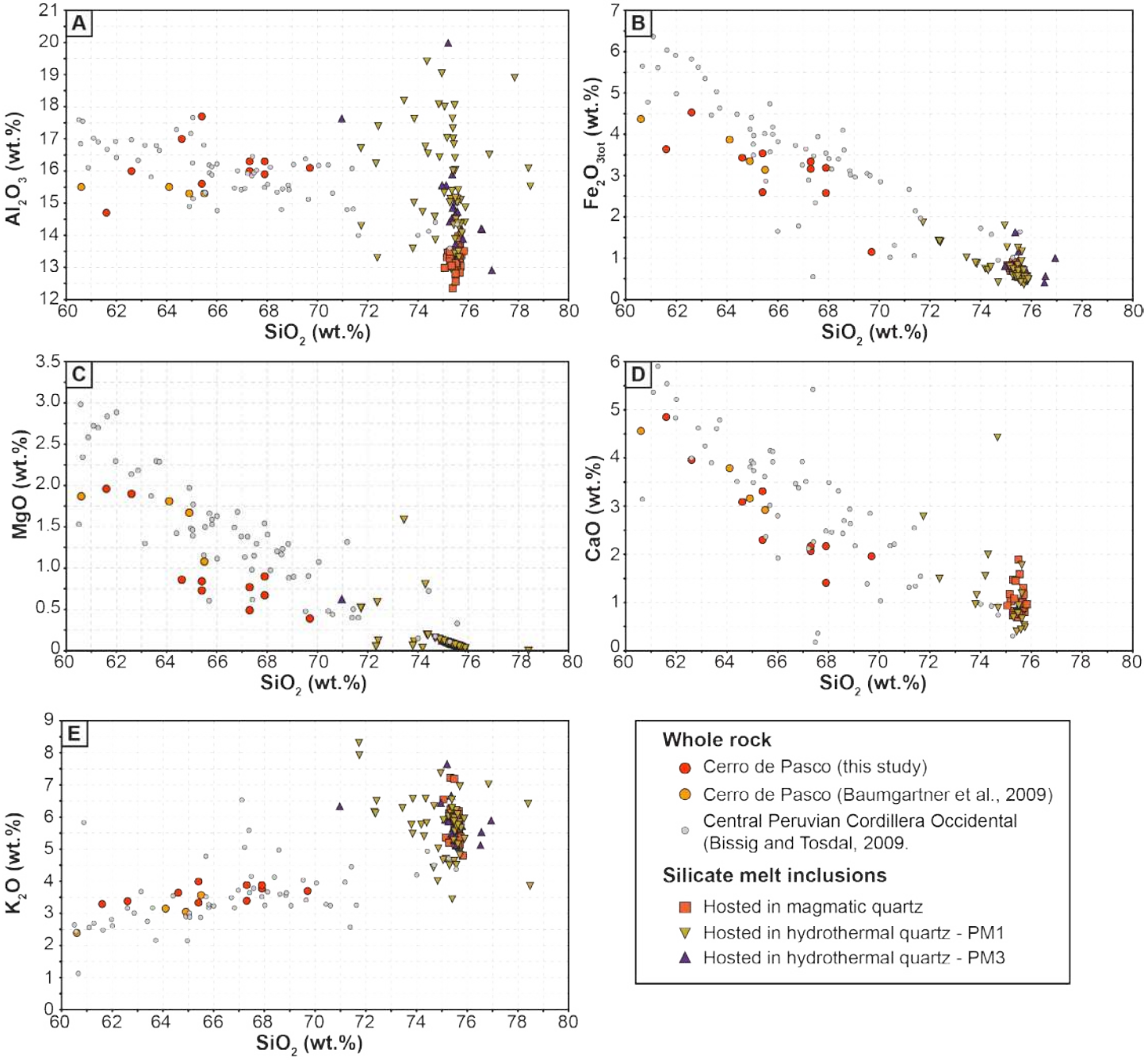
A
B
C
D
E
Al_2O_3 (wt.%)
Fe_2O_{3tot} (wt.%)
MgO (wt.%)
CaO (wt.%)
K_2O (wt.%)
SiO_2 (wt.%)
Whole rock
Cerro de Pasco (this study)
Cerro de Pasco (Baumgartner et al., 2009)
Central Peruvian Cordillera Occidental (Bissig and Tosdal, 2009.
Silicate melt inclusions
Hosted in magmatic quartz
Hosted in hydrothermal quartz - PM1
Hosted in hydrothermal quartz - PM3

Figure 11:

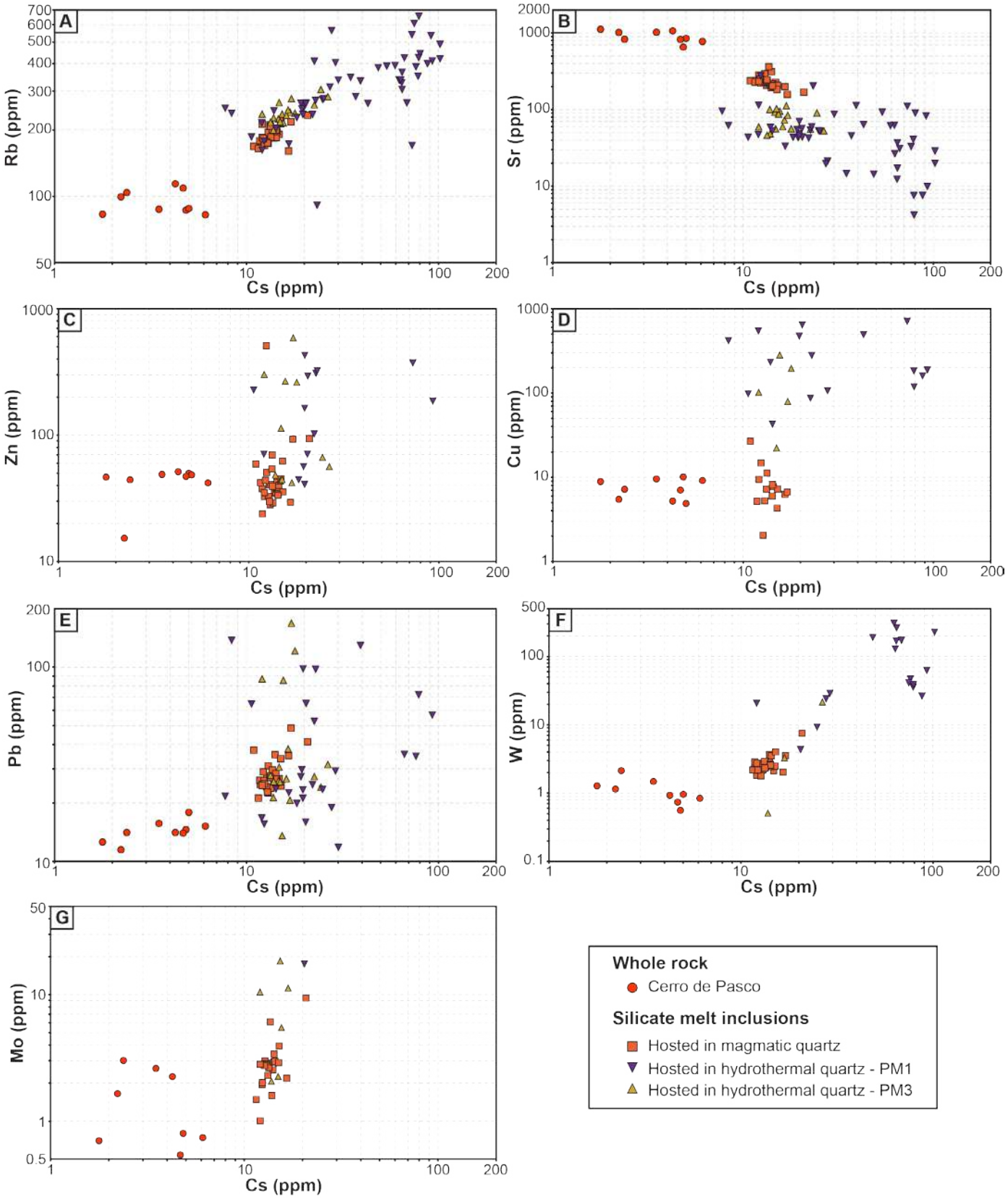
A
Rb (ppm)
Cs (ppm)
B
Sr (ppm)
Cs (ppm)
C
Zn (ppm)
Cs (ppm)
D
Cu (ppm)
Cs (ppm)
E
Pb (ppm)
Cs (ppm)
F
W (ppm)
Cs (ppm)
G
Mo (ppm)
Cs (ppm)
Whole rock
Cerro de Pasco
Silicate melt inclusions
Hosted in magmatic quartz
Hosted in hydrothermal quartz - PM1
Hosted in hydrothermal quartz - PM3

Figure 12:

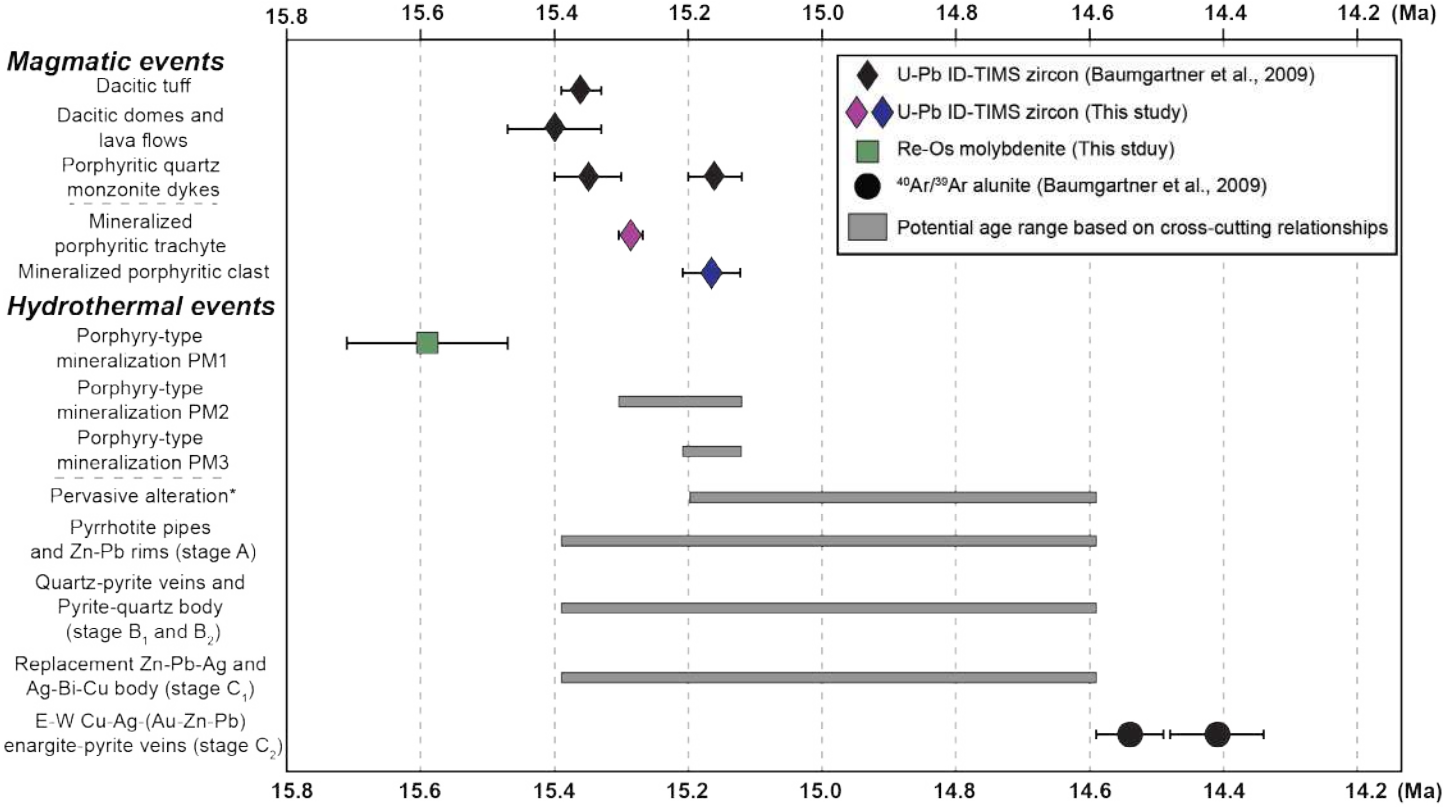

(*) Pyrophyllite-quartz-pyrite alteration / Illite-smectite-muscovite-pyrite alteration /chlorite-pyrite-calcite alteration

Figure 13:

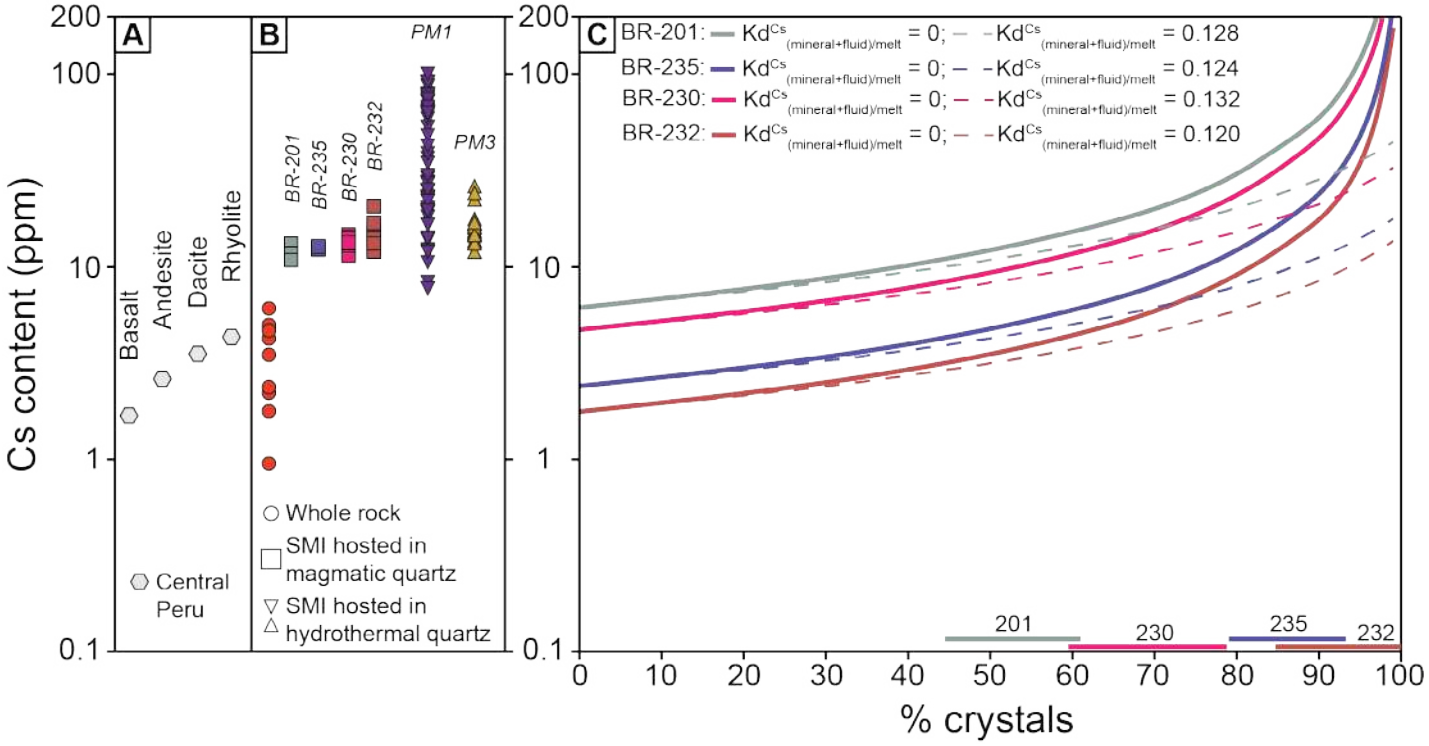
A
B
C
Cs content (ppm)
200
100
10
1
0.1
Basalt
Andesite
Dacite
Rhyolite
Central Peru
BR-201
BR-235
BR-230
BR-232
PM1
PM3
Whole rock
SMI hosted in magmatic quartz
SMI hosted in hydrothermal quartz
BR-201: Kd^Cs (mineral+fluid)/melt = 0; – Kd^Cs (mineral+fluid)/melt = 0.128
BR-235: Kd^Cs (mineral+fluid)/melt = 0; – Kd^Cs (mineral+fluid)/melt = 0.124
BR-230: Kd^Cs (mineral+fluid)/melt = 0; – Kd^Cs (mineral+fluid)/melt = 0.132
BR-232: Kd^Cs (mineral+fluid)/melt = 0; – Kd^Cs (mineral+fluid)/melt = 0.120
201
230
235
232
0
10
20
30
40
50
60
70
80
90
100
% crystals

Figure 14

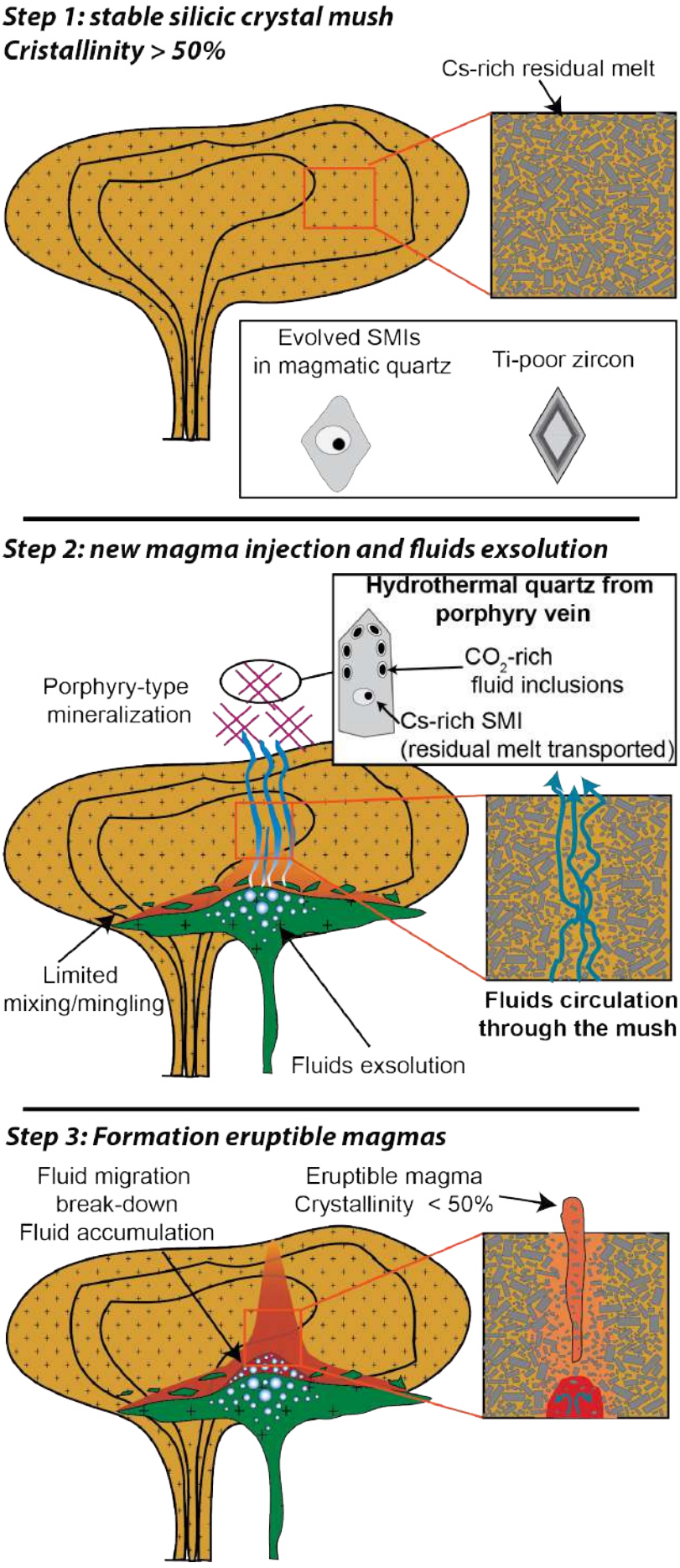
Step 1: stable silicic crystal mush
Cristallinity > 50%
Cs-rich residual melt
Evolved SMIs
in magmatic quartz
Ti-poor zircon
Step 2: new magma injection and fluids exsolution
Hydrothermal quartz from
porphyry vein
CO2-rich
fluid inclusions
Cs-rich SMI
(residual melt transported)
Porphyry-type
mineralization
Limited
mixing/mingling
Fluids exsolution
Fluids circulation
through the mush
Step 3: Formation eruptible magmas
Fluid migration
break-down
Fluid accumulation
Eruptible magma
Crystallinity < 50%